

NRC Publications Archive Archives des publications du CNRC

The massive survey. II. Stellar population trends out to large radius in massive early-type galaxies

Greene, Jenny E.; Janish, Ryan; Ma, Chung-Pei; McConnell, Nicholas J.; Blakeslee, John P.; Thomas, Jens; Murphy, Jeremy D.

This publication could be one of several versions: author's original, accepted manuscript or the publisher's version. / La version de cette publication peut être l'une des suivantes : la version prépublication de l'auteur, la version acceptée du manuscrit ou la version de l'éditeur.

For the publisher's version, please access the DOI link below. / Pour consulter la version de l'éditeur, utilisez le lien DOI ci-dessous.

Publisher's version / Version de l'éditeur:

<https://doi.org/10.1088/0004-637X/807/1/11>

The Astrophysical Journal, 807, 1, 2015-06-24

NRC Publications Archive Record / Notice des Archives des publications du CNRC :

<https://nrc-publications.canada.ca/eng/view/object/?id=1ce254a0-05bc-48a0-bf42-b1721a3b778d>

<https://publications-cnrc.canada.ca/fra/voir/objet/?id=1ce254a0-05bc-48a0-bf42-b1721a3b778d>

Access and use of this website and the material on it are subject to the Terms and Conditions set forth at

<https://nrc-publications.canada.ca/eng/copyright>

READ THESE TERMS AND CONDITIONS CAREFULLY BEFORE USING THIS WEBSITE.

L'accès à ce site Web et l'utilisation de son contenu sont assujettis aux conditions présentées dans le site

<https://publications-cnrc.canada.ca/fra/droits>

LISEZ CES CONDITIONS ATTENTIVEMENT AVANT D'UTILISER CE SITE WEB.

Questions? Contact the NRC Publications Archive team at

PublicationsArchive-ArchivesPublications@nrc-cnrc.gc.ca. If you wish to email the authors directly, please see the first page of the publication for their contact information.

Vous avez des questions? Nous pouvons vous aider. Pour communiquer directement avec un auteur, consultez la première page de la revue dans laquelle son article a été publié afin de trouver ses coordonnées. Si vous n'arrivez pas à les repérer, communiquez avec nous à PublicationsArchive-ArchivesPublications@nrc-cnrc.gc.ca.

THE MASSIVE SURVEY. II. STELLAR POPULATION TRENDS OUT TO LARGE RADIUS IN MASSIVE EARLY-TYPE GALAXIES

JENNY E. GREENE¹, RYAN JANISH², CHUNG-PEI MA³, NICHOLAS J. MCCONNELL⁴, JOHN P. BLAKESLEE⁵, JENS THOMAS⁶, AND JEREMY D. MURPHY⁷

¹Department of Astrophysics, Princeton University, Princeton, NJ 08544, USA

²Department of Physics, University of California, Berkeley, CA 94720, USA

³Department of Astronomy, University of California, Berkeley, CA 94720, USA

⁴Institute for Astronomy, University of Hawaii at Manoa, Honolulu, HI 96822, USA

⁵Dominion Astrophysical Observatory, NRC Herzberg Institute of Astrophysics, Victoria, BC V9E 2E7, Canada

⁶Max Planck-Institute for Extraterrestrial Physics, Giessenbachstr. 1, D-85741 Garching, Germany

⁷IXL Learning, 777 Mariners Island Blvd., Suite 600, San Mateo, CA 94404

Received 2015 February 24; accepted 2015 April 27; published 2015 June 24

ABSTRACT

We examine stellar population gradients in ~ 100 massive early-type galaxies spanning $180 < \sigma_* < 370$ km s⁻¹ and M_K of -22.5 to -26.5 mag, observed as part of the MASSIVE survey. Using integral-field spectroscopy from the Mitchell Spectrograph on the 2.7 m telescope at McDonald Observatory, we create stacked spectra as a function of radius for galaxies binned by their stellar velocity dispersion, stellar mass, and group richness. With excellent sampling at the highest stellar mass, we examine radial trends in stellar population properties extending to beyond twice the effective radius ($\sim 2.5 R_e$). Specifically, we examine trends in age, metallicity, and abundance ratios of Mg, C, N, and Ca, and discuss the implications for star formation histories and elemental yields. At a fixed physical radius of 3–6 kpc (the likely size of the galaxy cores formed at high redshift), stellar age and $[\alpha/\text{Fe}]$ increase with increasing σ_* and depend only weakly on stellar mass, as we might expect if denser galaxies form their central cores earlier and faster. If we instead focus on 1–1.5 R_e , the trends in abundance and abundance ratio are washed out, as might be expected if the stars at large radius were accreted by smaller galaxies. Finally, we show that when controlling for σ_* , there are only very subtle differences in stellar population properties or gradients as a function of group richness; even at large radius, internal properties matter more than environment in determining star formation history.

Key words: galaxies: elliptical and lenticular, cD – galaxies: evolution – galaxies: kinematics and dynamics – galaxies: stellar content

1. INTRODUCTION

The assembly history of elliptical galaxies remains a major unsolved problem for galaxy evolution. Recent observations point to dramatic size evolution of the most massive galaxies from $z \approx 2$ to the present (e.g., van Dokkum et al. 2008; van der Wel et al. 2008; Patel et al. 2013; van der Wel et al. 2014). The extent to which these trends require late-stage minor mergers (e.g., Oser et al. 2012) or can be explained by the addition of larger, younger galaxies at later times (Valentinuzzi et al. 2010; Newman et al. 2012; Barro et al. 2013) remains a topic of ongoing debate. Information lurking in the faint outer parts of present-day massive ellipticals can complement high-redshift measurements. Radial gradients in stellar populations distinguish when and how the stars at large radius were formed (e.g., White 1980; Kobayashi 2004; Greene et al. 2013; Hirschmann et al. 2015), while the kinematics of the stars (e.g., V/σ_* , the level of radial anisotropy, etc.) contain clues about how these stars entered the halo (e.g., Arnold et al. 2014; Naab et al. 2014; Raskutti et al. 2014; Röttgers et al. 2014; Wu et al. 2014).

Here we focus on the average radial trends in stellar populations of early-type galaxies using our ambitious survey of the hundred most MASSIVE galaxies within 100 Mpc (Ma et al. 2014). Observations of the stellar populations in elliptical galaxy outskirts are challenging, since their surface brightnesses drop steeply with radius. Despite more than thirty years of effort, most observations of stellar population gradients do

not extend much beyond the half-light radius (Spinrad & Taylor 1971; Faber et al. 1977; Gorgas et al. 1990; Fisher et al. 1995; Kobayashi & Arimoto 1999; Ogando et al. 2005; Brough et al. 2007; Baes et al. 2007; Annibali et al. 2007; Sánchez-Blázquez et al. 2007; Rawle et al. 2008; Kuntschner et al. 2010; McDermid et al. 2015; Oliva-Altamirano et al. 2015). Resolved stellar population studies have uncovered a low-metallicity halo component at very large radius, but only in a handful of nearby galaxies (e.g., Kalirai et al. 2006; Harris et al. 1999; Rejkuba et al. 2005; Harris et al. 2007; Crnojević et al. 2013; Pastorello et al. 2014; Peacock et al. 2015; Williams et al. 2015). There are also a few long-slit observations that extend to large radius (Carollo et al. 1993; Carollo & Danziger 1994; Mehlert et al. 2003; Kelson et al. 2006; Spolaor et al. 2010; Pu et al. 2010; Pu & Han 2011). Even integral-field spectrographs, now widely used for the study of spatially resolved galaxy properties (Emsellem et al. 2004; Cappellari et al. 2006, 2012; Sarzi et al. 2006), include few observations that extend beyond the half-light radius in integrated light (Weijmans et al. 2009; Murphy et al. 2011).

The ~ 100 galaxies analyzed here represent a significant improvement over previous work. Using coadded spectra as a function of radius, we will investigate whether radial gradients depend not only on stellar velocity dispersion, but also on other intrinsic galaxy properties such as stellar mass and environmental density. We find a hint that at fixed σ_* , galaxies residing in higher densities are older and more α -element enhanced, but

we see no evidence for differing gradients for galaxies in low and high densities.

We present the sample in Section 2, the observations and data reduction in Section 3, our stellar population analysis in Section 4, and the radial variations in stellar populations in Section 5. We summarize our findings and conclude in Section 6. Throughout we assume a concordance cosmology with $H_0 = 70 \text{ km s}^{-1} \text{ Mpc}^{-1}$, $\Omega_M = 0.3$, and $\Omega_\Lambda = 0.7$ (Dunkley et al. 2009).

2. SAMPLE

The MASSIVE sample selection is described in detail in Ma et al. (2014). For completeness, we summarize the sample selection briefly here. MASSIVE is a volume-limited sample of the 116 most massive galaxies within 108 Mpc. The galaxies are selected from the 2MASS Redshift Survey (Huchra et al. 2012), using a total K -band magnitude limit of $M_K < -25.3 \text{ mag}$ (roughly $10^{11.5} M_\odot$). Using the Hyperleda database (Paturel et al. 2003), we apply a morphological cut to remove large spiral and interacting galaxies. The resulting 116 galaxies span a wide range of stellar velocity dispersion ($\sim 180\text{--}400 \text{ km s}^{-1}$) and, based on the group catalog of Crook et al. (2007), are found in a wide array of environments, from “field” galaxies with no $\sim L^*$ companions to rich clusters (Coma, Perseus, and Virgo). In this paper, we include 49 MASSIVE galaxies with large-format integral-field spectrograph observations in hand. While we are also obtaining high spatial resolution integral field spectroscopy for a subset of galaxies for black hole mass determinations (e.g., McConnell et al. 2012), this paper deals exclusively with the Mitchell data.

In addition to the ongoing MASSIVE survey, we include here a sample of lower-mass galaxies (Greene et al. 2013) selected directly from the Sloan Digital Sky Survey (SDSS; York et al. 2000) and observed with an identical set-up with the Mitchell Spectrograph. As the selection was different, we briefly review it here (see also Greene et al. 2012; Raskutti et al. 2014). Since the spectral resolution of the Mitchell Spectrograph is $\sigma_{\text{inst}} \approx 150 \text{ km s}^{-1}$ at 4000 \AA , we select galaxies with dispersion measurements from the SDSS that are greater than this value. Individual fibers are $4''2$ in diameter, and so we aim for galaxies with effective radii at least twice as large. Galaxies with distances of 40–95 Mpc are large enough to be well-resolved but small enough to fit into one pointing. We use a color selection of $u - r > 2.2$ (Strateva et al. 2001), which preferentially selects early-type galaxies, and then remove the few edge-on disk galaxies by hand, but keep S0 galaxies. These 46 galaxies are of uniformly lower stellar mass than those in MASSIVE. Taken together, the sample galaxies span a range of $-22.5 < M_K < -26.5$ Vega mag. The sample properties for the 95 galaxies (49 from MASSIVE) are summarized in Figure 1.

3. OBSERVATIONS AND DATA REDUCTION

The majority of the galaxies presented here were observed over ten observing runs between 2011 September and 2014 April. There are an additional four galaxies taken earlier as part of the PhD thesis of Jeremy Murphy (Murphy et al. 2011) and four taken by Nicholas McConnell (McConnell et al. 2012). All of these data were taken with the George and Cynthia Mitchell Spectrograph (the Mitchell Spectrograph, formerly

VIRUS-P; Hill et al. 2008) on the 2.7 m Harlan J. Smith telescope at McDonald Observatory. The Mitchell Spectrograph is an integral-field spectrograph with 246 fibers subtending $4''2$ each and covering a $107'' \times 107''$ field of view with a one-third filling factor. As such, the Mitchell Spectrograph is ideal for studying the low surface brightness outer parts of nearby galaxies (Blanc et al. 2009; Joachim et al. 2010; Murphy et al. 2011; Adams et al. 2012).

We utilize the blue setting of the Mitchell spectrograph with a resolution of $R \approx 850$ and spanning a wavelength range of $3550\text{--}5850 \text{ \AA}$. This resolution (roughly a FWHM of 5 \AA) delivers a dispersion of $\sim 1.1 \text{ \AA pixel}^{-1}$ and corresponds to $\sigma_* \approx 150 \text{ km s}^{-1}$ at 4300 \AA , our bluest Lick index, improving to $\sim 100 \text{ km s}^{-1}$ at the red end of the spectrum. Each galaxy was observed for a total of $\sim 2 \text{ hr}$ on source with one-third of the time spent at each of three dither positions to fill the field of view. Observations are interleaved with sky observations of 10 min duration. Initial data reduction is accomplished using the custom code Vaccine (Adams et al. 2011; Murphy et al. 2011). The details of our data reduction are described in Murphy et al. (2011), so we repeat only a brief overview for completeness here.

We first perform overscan and bias subtraction for all science and calibration frames. The fiber trace is determined from the twilight flats, taking into account curvature in the spatial direction and following the techniques of Kelson (2003) to avoid interpolation and thus correlated errors. Arcs are used to derive a wavelength solution with typical rms residual variations about this best-fit fourth-order polynomial between 0.05 and 0.1 \AA . The twilight flats are also used to construct the flat field, once the solar spectrum has been modeled and removed. The flat field is typically stable to < 0.1 pixels for typical thermal variations in the instrument. The flat field is then applied to all of the science frames to correct variations in the pixel-to-pixel responses, as well as the relative fiber-to-fiber variation, and the cross-dispersion profile shape for every fiber. The sky is modeled using off-galaxy sky frames observed with a sky-object-object-sky pattern. The sky frames are processed in the same manner as the science frames. In general, each sky nod is weighted equally, except for very cloudy conditions. Finally, cosmic rays are identified and masked.

We use software developed for the VENGA project (Blanc et al. 2009, 2013) for flux calibration and final processing. We observe flux calibration stars using a six-point dither pattern and derive a relative flux calibration in the standard way. We can test the wavelength dependence of the flux calibration by comparing the shape of the spectrum in the central fiber of the Mitchell Spectrograph with the SDSS spectrum for those galaxies with SDSS spectra. We find $\lesssim 10\%$ disagreement in nearly all cases, with no more than $\sim 15\%$ differences at worst. We then correct the default astrometric solutions using photometry, by deriving an astrometric match between each image and an SDSS (York et al. 2000) or PanSTARRS (Schlafly et al. 2012; Tonry et al. 2012; Magnier et al. 2013) image. Finally, all fibers are interpolated onto the same wavelength scale and combined into radial bins.

3.1. Effective Radii

In our previous work, we adopted the SDSS model radius (the de Vaucouleurs fit) as the effective radius (R_e). While there is considerable evidence that the shape of the light profile changes systematically with galaxy mass (e.g., Caon et al. 1993;

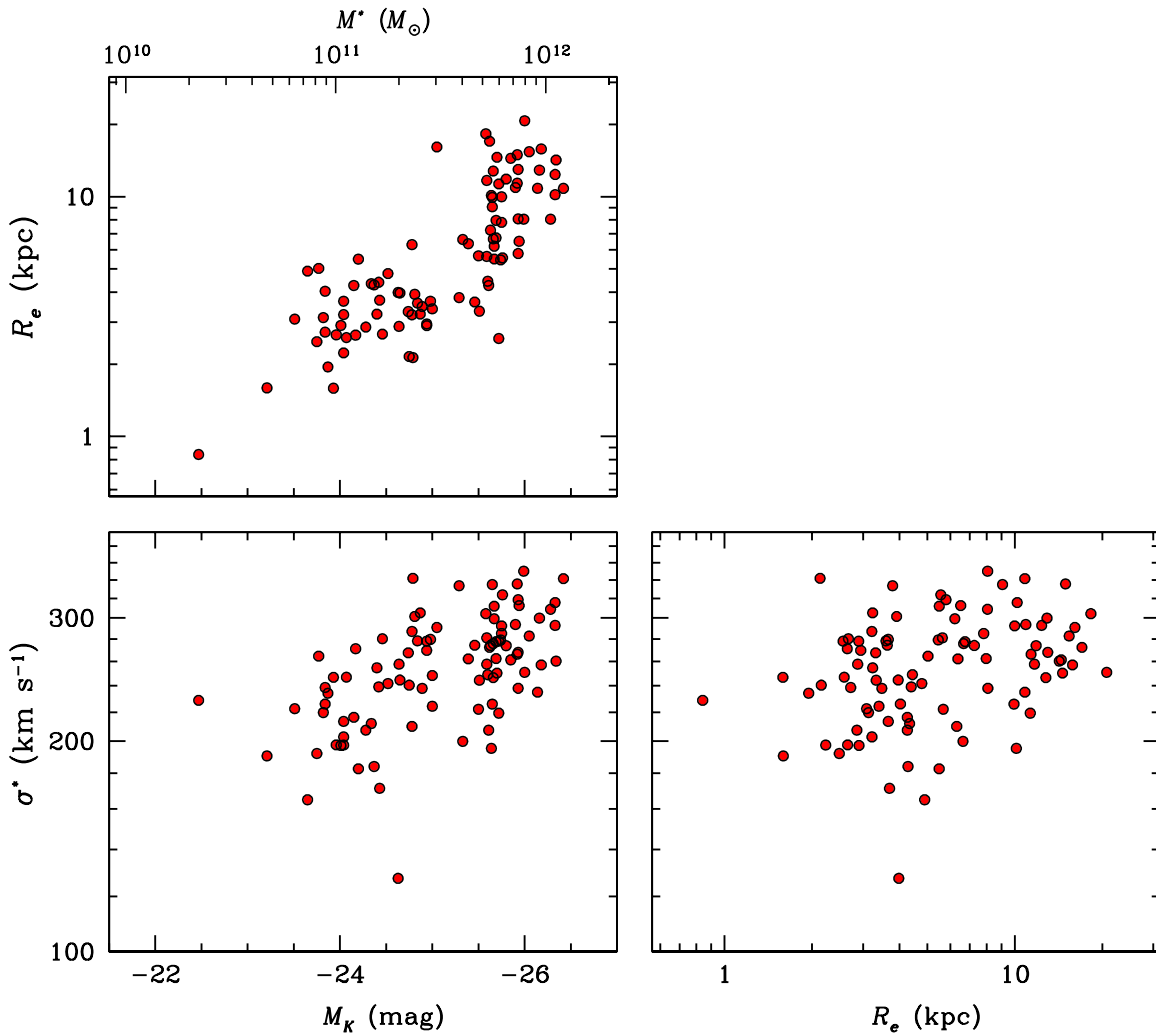


Figure 1. Distributions of basic structural properties for our sample. On bottom left, stellar velocity dispersion (σ_*) measured within the central fiber is plotted against M_K (mag; total magnitude) from 2MASS. On top left, we show effective radius, from the NSA catalog (or from 2MASS with a correction; Section 3.2) against M_K and on bottom right effective radius vs. stellar velocity dispersion.

Ferrarese et al. 2006; Kormendy et al. 2009), fitting the galaxies with a fixed Sérsic index of four has the benefit that we are less sensitive to both sky subtraction errors (Mandelbaum et al. 2005; Bernardi et al. 2007) and to the detailed shape of the light profile in the very faint wings (e.g., Lackner & Gunn 2012). In the case of MASSIVE, $\sim 1/3$ of the galaxies do not have SDSS imaging, so we adapt a size measurement from 2MASS (Jarrett et al. 2003). We use the median effective radius measured from the *JHK* band (see Equation (3) in Ma et al. 2014). The 2MASS size measurement tends to underestimate the galaxy sizes relative to the SDSS (Lauer et al. 2007; Kormendy et al. 2009). To put the size measurements on equal footing, Ma et al. (2014) fit a linear conversion between $R_{2\text{MASS}}$ and R_{SDSS} : $\log_{10}(R_{2\text{MASS}}) = 0.8 \log_{10}(R_{\text{SDSS}}) - 0.076$ (their Equation (4)). We use this relation to correct the 2MASS measurements to match the SDSS measurements.

3.2. Radial Bins

Spectra from individual fibers, with the exception of those at the very center of the IFU, have inadequate signal for stellar population studies. Therefore, all of our analysis is performed on binned spectra. We utilize two binning schemes here, in

both cases defining elliptical annuli based on the axis ratio measured by the SDSS or 2MASS. Since galaxies get larger as they get more massive, we make bins of width $0.5 R_e$. However, it is also interesting to look at trends as a function of physical size, and here we extend from 0–15 kpc in 3 kpc increments. For the physical bins, we use the central fiber as the central bin; while this central fiber corresponds to a different physical size for each system, it provides our highest spatial resolution bin.

3.3. Stellar Velocity Dispersion Measurements

Stellar velocity dispersions are required for measuring Lick indices. This is because at fixed intrinsic absorption, as the velocity dispersion increases, the measured equivalent width (EW) decreases. Thus, a correction must be applied to put all indices on the same scale. We also use the central stellar velocity dispersions to rank galaxies in constructing coadded spectra. Our central $4''.2$ fiber is similar to the SDSS fiber and thus easily compared with the literature. We use pPXF to measure the dispersions (Cappellari & Emsellem 2004). We compare our σ_* measurements with SDSS measurements when available or our compiled literature values (Ma et al. 2014)

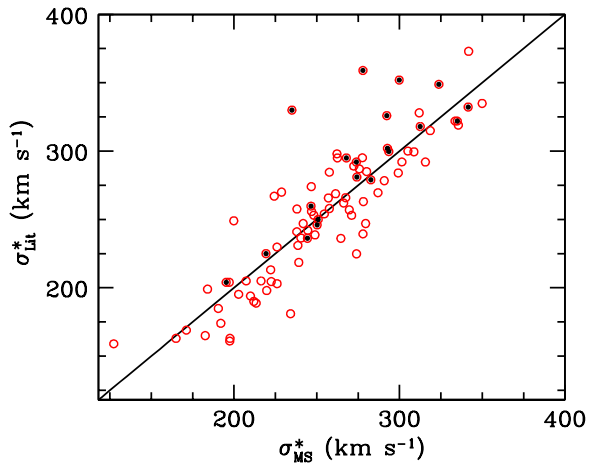


Figure 2. Stellar velocity dispersions (σ_*) measured within the central $4''2$ Mitchell fiber are compared with literature values. Open symbols have literature measurements from the SDSS, while filled symbols are from Hyperleda. The overall agreement is quite good, with $(\sigma_{\text{MS}} - \sigma_{\text{Lit}}) / \sigma_{\text{Lit}} = 0.01 \pm 0.09$.

derived from the Hyperleda database (Paturel et al. 2003). We find very good agreement, with the median $(\sigma_{\text{MS}} - \sigma_{\text{Lit}}) / \sigma_{\text{Lit}} = 0.01 \pm 0.09$. That is, we see no systematic offset between the two sets of measurements and a scatter of 9%. We compare our measurements with the literature in Figure 2. As discussed in van den Bosch et al. (2015), there is some excess scatter at the high dispersion end, specifically when we compare with Hyperleda. However, we find better agreement with Hyperleda than reported by van den Bosch et al. predominantly due to recent (post-2013) changes in Hyperleda. We have 51 objects in common with the van den Bosch HET catalog, and we also find reasonable agreement with their σ_* measurements, with $(\sigma_{\text{MS}} - \sigma_{\text{HET}}) / \sigma_{\text{HET}} = -0.03 \pm 0.07$. Throughout, σ_* refers to our measurements from the central fiber unless otherwise specified.

4. ANALYSIS

4.1. Stellar Population Modeling Approach

We use Lick indices as a tool to trace the stellar populations. Lick indices were developed as a way to extract stellar population information from spectra without flux calibration, but still circumvent classic age–metallicity degeneracies (Burstein 1985; Faber et al. 1985; Worthey et al. 1992; Trager et al. 1998). The Lick indices are narrow regions of the spectra (typically $\sim 20 \text{ \AA}$ wide) that are dominated by a single element and thus are predominantly sensitive to orthogonal aspects of the stellar population properties; $H\beta$ is sensitive to age, Fe indices to $[\text{Fe}/\text{H}]$, and so on. It is important to bear in mind that at the velocity dispersion of our target galaxies ($200\text{--}400 \text{ km s}^{-1}$) all indices are blends of multiple elements. See, for example, Table 1 in Graves & Schiavon (2008) for the primary elements that dominate the Lick indices used in this work.

Lick indices are still widely used in the literature as they mitigate difficulties in modeling the effects of abundance ratio changes (e.g., Worthey et al. 1994; Gallazzi et al. 2005). Trager et al. (2000b, 2000a) developed a technique to derive index responses from stellar atmosphere models, such that even if the full spectrum cannot be calculated, the index EW changes due to changing abundance ratios can be incorporated into an analysis of line EWs. On the other hand, the current generation

of full spectral synthesis codes are very sophisticated (e.g., Vazdekis et al. 2010; Conroy & van Dokkum 2012) and have been designed to fit non-solar abundance ratios.

For reference, we review the main indices that we use to derive the basic stellar population parameters. The reader is referred to Graves & Schiavon (2008) for more detailed information. We use *lick_ew* (Graves & Schiavon 2008) to measure the Lick indices and the stellar population modeling code *EZ_Ages* (Graves & Schiavon 2008) to convert the Lick indices to physical parameters (age, $[\text{Fe}/\text{H}]$, $[\alpha/\text{Fe}]$). The code works on a hierarchy of index pairs, starting with $H\beta$ and $\langle \text{Fe} \rangle$, and iteratively solves for the age, abundance and abundance ratios. The models of Schiavon (2007) include abundance ratio differences using the response functions of Korn et al. (2005). For a different inversion methodology see Thomas et al. (2011) or for full spectral fitting comparisons see Conroy et al. (2014).

As emphasized by Schiavon (2007), because we do not directly measure the oxygen abundance and oxygen is the most abundant heavy element, it is misleading to quote total metallicity. Instead, we quote $[\text{Fe}/\text{H}]$, which is directly inferred from the Fe indices. If we assume that $[\text{O}/\text{Fe}]$ tracks $[\text{Mg}/\text{Fe}]$, then we can use the latter to infer $[\text{Z}/\text{H}]$. We will generally assume that O and Mg follow similar trends as they are both α elements, and thus use $[\text{Mg}/\text{Fe}]$ interchangeably with $[\alpha/\text{Fe}]$. Based on the same assumption, we also will use the conversion from Trager et al. (2000b): $[\text{Z}/\text{H}] = [\text{Fe}/\text{H}] + 0.94[\alpha/\text{Fe}]$ to calculate the metallicity. For alternate approaches to modeling oxygen using Lick indices, see Johansson et al. (2012) or Worthey et al. (2014). In our default runs, we utilize the α -enhanced isochrone from Salasnich et al. (2000) and the default assumption that $[\text{O}/\text{Fe}] = 0.5$ to match the α -enhanced isochrone value.

Carbon is roughly half as abundant by number as oxygen at solar abundances (Asplund et al. 2009). We derive $[\text{C}/\text{Fe}]$ from the C_{24668} index (e.g., Tripicco & Bell 1995; Trager et al. 1998; Graves et al. 2007; Johansson et al. 2012). Because the amount of C locked into CO depends on the oxygen abundance, as we lower the assumed O abundance, the inferred C abundance drops commensurately (Serven et al. 2005). We will quantify the magnitude of this effect below.

Nitrogen (one-tenth the O abundance by number in the Sun) is then derived from CN1 (4143–4178 \AA) once we have a C abundance. As discussed in Greene et al. (2013), there are some uncertainties associated with CN due to the low signal-to-noise ratio (S/N) at the blue end of the spectrum, but our nuclear CN measurements match those from the SDSS spectra of the same galaxies (our Mitchell indices are $0.01 \pm 0.02 \text{ mag}$ lower than the SDSS measurements), giving us some confidence in these measurements.

Finally, the Ca abundance (one-hundredth the C abundance by number in the Sun) is based on the Ca4227 index (4223.5–4236.0 \AA ; Worthey 1998). This index is blended with CN, and thus the $[\text{Ca}/\text{Fe}]$ measurement is most uncertain, as it is dependent on both the $[\text{C}/\text{Fe}]$ and $[\text{N}/\text{Fe}]$ measurements. Others have used Ca H + K (Serven et al. 2005; Worthey et al. 2014) or the Ca Triplet at 8600 \AA , where the last is also sensitive to the dwarf-to-giant ratio (e.g., Cenarro et al. 2004).

Since the Lick indices are very sensitive to small errors in sky subtraction and other small-scale errors, we construct stacked spectra and measure the average radial trends in the Lick indices and resulting stellar populations.

4.2. Equivalent Widths and Emission Line Corrections

There are a number of systematic effects that may impact the EWs. One relates to the velocity dispersion: while the default dispersion corrections within *lick_ew* were verified originally over the range $\sigma_* = 250\text{--}300 \text{ km s}^{-1}$, some of our galaxies exhibit even larger σ_* . We therefore check our dispersion corrections using simple stellar population models from (Conroy & van Dokkum 2012), broadened over the full observed range of σ_* . The Lick indices that we recover using the default *lick_ew* corrections agree with the input values within 0.02 \AA for an α -enhanced model with a Salpeter IMF, which is a good approximation to our galaxies. The corrections are a weak function of stellar population parameters, but only at the hundredths of an \AA level, which is small compared to our other sources of systematic error.

A larger correction must be made for low-level emission that can fill in the absorption lines and artificially lower their EWs. Weak emission from warm ionized gas is very common in the centers of elliptical galaxies (Sarzi et al. 2010; Yan & Blanton 2012), and small amounts of line infill can lead to significant errors in recovered parameters. Even 0.1 \AA errors in $H\beta$ EW can lead to errors of $\sim 1\text{--}2 \text{ Gyr}$ in the modeling (e.g., Schiavon 2007).

Given the very low emission levels and the large uncertainties involved, we compare two methods for determining the levels of $[O\text{ III}]$ and $H\beta$ emission. In Greene et al. (2012), we utilized pPXF+GANDALF developed by M. Sarzi (Sarzi et al. 2006) and M. Cappellari (Cappellari & Emsellem 2004) to simultaneously model the stellar absorption and emission lines. GANDALF is very robust for well-detected lines, but under-constrained for very weak emission. Following Greene et al. (2013), we also fit each spectrum with an empirical template drawn from the composite spectra of Graves et al. (2010). We then fit the $[O\text{ III}]$ emission in the residual spectrum, and subtract both $[O\text{ III}]$ and $H\beta$, assuming that the $H\beta$ emission is 70% of the $[O\text{ III}]$ flux (measured to within a factor of two, Trager et al. 2000b; Graves et al. 2007). We then iterate these fits until the emission line flux has converged. In addition, we search for residuals around strong sky lines at 5200 and 5460 \AA .

From our iterative fits, and focused on the galaxy centers for simplicity, roughly two-thirds of the galaxies have low-level $H\beta$ emission detected, with a median EW of 0.2 \AA , and a maximum of 1 \AA (calculated for those galaxies with detected $H\beta$). The Gandalf measurements do not correlate very strongly with our iterative fits. In the GANDALF fits, only half of the galaxies have detections, with a median EW is 0.2 \AA and a maximum $H\beta$ EW of 1.7 \AA . As a means of quantifying our systematic errors, we rerun the stacking analysis described below on the Gandalf-subtracted spectra. As expected, only the stellar age changes significantly, being $\sim 3 \text{ Gyr}$ lower in the Gandalf stacks. But all other stellar population properties are virtually identical (with the $[\text{Fe}/\text{H}]$ shifting higher by a small amount to compensate the shift in stellar age). Thus, we present results based on the iterative fits, but we caution that there is a rather large systematic uncertainty in the absolute stellar age. All other stellar population properties are robust to this modeling difficulty, and in general the relative ages are robust as well. We are currently working on more robust gas detection schemes using all lines in the spectra (V. Pandya et al. 2015, in preparation).

We then use *lick_ew* (Graves & Schiavon 2008) on the emission-line corrected spectra. The indices are on a modified Lick system presented by Schiavon (2007) based on flux-calibrated spectra. In order to demonstrate that we are on the same system, we compare the Lick indices from the flux-calibrated SDSS spectra (the inner $3''$) with those from the central $4''/2$ fiber in our data. There is no net offset between the two sets of indices in any case, with $\langle (H\beta \text{ EW}_S - H\beta \text{ EW}_{MS}) / H\beta \text{ EW}_{MS} \rangle = 0.08 \pm 0.17$, where S is SDSS and MS is the Mitchell Spectrograph. $\langle \text{Fe} \rangle$ and Mgb each have a scatter of only $\sim 10\%$ and even smaller net offsets.

4.3. Composite Spectra

While measuring Lick indices is a very powerful technique for high S/N spectra, at the large radii that we are working, systematic effects such as small errors in sky subtraction and flux calibration can begin to cause large uncertainties in the Lick indices measured from individual objects. Stacked spectra average over sky subtraction and flux calibration errors in individual systems, which occur at different wavelengths in each galaxy rest-frame (e.g., Graves et al. 2009; Yan 2011). Of course, variations in stellar populations at a given σ_* or mass are expected based on differences in accretion history (e.g., Hirschmann et al. 2015) and we are quite interested in these differences, particularly as a function of the dynamical properties of the galaxies. We plan to implement full spectral fitting in the near future, which is more robust at low S/N (e.g., Choi et al. 2014).

We know that stellar population properties are a strong function of σ_* (e.g., Worthey et al. 1992; Bender et al. 1993; Trager et al. 2000a; Graves et al. 2009). Thus, we first divide the galaxies into four stellar velocity dispersion bins using our pPXF measurements to the central fiber. Of the 95 galaxies in our sample, we exclude eight. Most of these are from the low-mass sample and have a bright star in the foreground making it difficult to reach a reasonable S/N. NGC1167 in the MASSIVE sample is excluded because it may be a face-on disk galaxy. We will treat it more carefully in future work. The bins have $\sigma_* < 220 \text{ km s}^{-1}$ (15 objects), $220 < \sigma_* < 250 \text{ km s}^{-1}$ (21 objects), $250 < \sigma_* < 290 \text{ km s}^{-1}$ (33 objects), and all those higher than $\sigma_* > 290 \text{ km s}^{-1}$ (18 objects). Stacked spectra within $0.5 R_e$ are shown in Figure 3. The resulting stellar population parameters are shown in Figure 4. We reach different physical radii for different bins as we run out of signal for the smaller and lower-mass galaxies. Also, the total number of galaxies included in the largest radial bin is typically $\sim 30\%$ smaller than the centers, as various systematic effects such as foreground star contamination grow more severe at low flux levels.

Below, we will also bin on stellar mass and group richness. While the detailed bins are different, the stacking technique described here is the same for these different sets of bins.

To create the stack, we coadd the emission-line-subtracted spectra. We interpolate the rest-frame spectra onto a common wavelength grid. To ensure we know the dispersion of the final stacked spectrum, we then smooth each galaxy to a value that is 30% higher than the upper σ_* limit of each bin. This smoothing ensures that all galaxies go into the stack with the same effective dispersion. With this approach, we minimize small errors due to dispersion corrections to the Lick indices. An alternate procedure would be to smooth all templates, in all bins, to a high dispersion (e.g., 400 km s^{-1}). We find very small

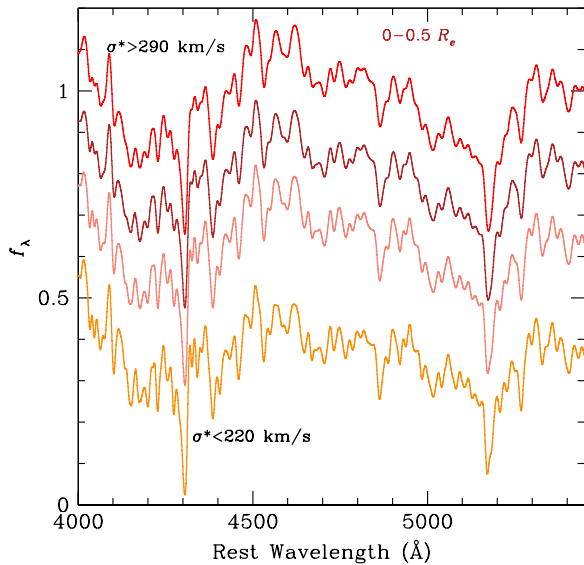


Figure 3. Coadded spectra within $0.5 R_e$, for stellar velocity dispersion stacks starting from $\sigma_* < 220 \text{ km s}^{-1}$ (bottom) to $\sigma_* > 290 \text{ km s}^{-1}$ (top). Each spectrum has been normalized to unity as described in the text, and the flux density offsets are arbitrarily applied for display purposes. In creating the stacks, each galaxy was smoothed to a value 30% more than the upper end of the dispersion range in creating the stack.

($< 0.01 \text{ \AA}$) differences in the resulting indices if we adopt the latter approach, again confirming that our dispersion corrections are working (Section 4.2). When we make bins in M_K below, because of the wide range of σ_* in each bin, we smooth all bins to 400 km s^{-1} .

We remove the continuum by dividing each spectrum by a heavily smoothed version of itself. This step simultaneously normalizes all spectra to the same level and ensures that differences in continuum shape (whether real or due to small errors in sky subtraction or flux calibration) do not impact the final line strengths. We then calculate the median flux at each pixel, with rejection, although we get very similar results using the biweight estimator (Beers et al. 1990). We experiment with multiplying the coadded spectrum by the median continuum before measuring indices, but the changes to the Lick indices are negligible.

4.4. Uncertainties

To determine the level of variation in the composite spectra, we generate 100 boot-strapped composite spectra by randomly drawing from the total list of galaxies in that bin, with replacement. We measure Lick indices from each of these 100 trial spectra. We then assign errors on the Lick indices that enclose 68% of the Lick indices measured from the 100 trials. Therefore, the size of the error is most directly related to the variance in parameters over the population in that bin, rather than measurement or modeling uncertainty. The systematic uncertainties are not shown. Age measurements have large systematic uncertainties due to emission infill (Section 4.2), while nitrogen and calcium are particularly uncertain due to their dependence on blue spectral features and assumed carbon and oxygen abundances.

In general, we report the measurement from the primary stacked spectrum, and the errors derived from the boot-strapped spectra. There are a few cases where the Lick index measured from the primary stacked spectrum does not fall within the

stellar population grids (usually because the $H\beta$ index is slightly too low). In these cases, we use the median index value from the 100 trials as the final answer. These cases are indicated with open symbols.

5. RADIAL VARIATIONS IN STELLAR POPULATIONS

5.1. Bins of σ_*

In Figure 4 we show radial trends in the measured age, $[\text{Fe}/\text{H}]$, and abundance ratios as a function of physical (left) and R_e -scaled (right) radii. Our default models make the assumption that $[\text{O}/\text{Fe}]$ is enhanced like $[\text{Mg}/\text{Fe}]$, since they are both α elements. However, in Figure 4 we indicate with dashed lines the C, N, and Ca abundances that result for an assumed solar $[\text{O}/\text{Fe}]$. While the zeropoints of $[\text{C}/\text{Fe}]$ and $[\text{N}/\text{Fe}]$ both decline, the radial trends will not change unless $[\text{O}/\text{Fe}]$ (unlike $[\text{Mg}/\text{Fe}]$) changes with radius.

We fit a power-law relation between radius and each stellar population property. We anchor the relation at the center of our radial coverage. Eventually, when we have reliable K -band light profiles for each galaxy, we will calculate mass-weighted stellar population properties, but at present, for a given stellar population property X we fit a log-linear relationship: $X = A \log(R/R_3) + B$, where R_3 is the third bin, corresponding either to 3–6 kpc or $1-1.5 R_e$. The quantity A represents the radial gradient per log radius. The quantity B represents an effective stellar population property at the center of our radial coverage. The fits to A and B for each relation are shown in Tables 1 and 2.

The strongest radial gradients are found between $[\text{Fe}/\text{H}]$ and $[\text{C}/\text{Fe}]$, which both decline with radius. Age shows a decline in the highest dispersion bin, but because that effect is weaker when we use the alternate emission line correction, we treat age gradients with extra caution. All other abundance ratios measured here are consistent with remaining flat over the full radial range, aside from a 2σ increase in $[\text{Ca}/\text{Fe}]$ at large radius that is only seen in the largest σ_* bin.

We turn to trends between stellar populations and σ_* . Our central bins are shown as open circles in Figure 5. We recover well-known trends between stellar population properties and stellar velocity dispersion for galaxy centers. Galaxies with higher stellar velocity dispersions have older stellar ages and higher $[\text{Mg}/\text{Fe}]$ and $[\text{C}/\text{Fe}]$ ratios (e.g., Trager et al. 2000b; Worthey 2004; Thomas et al. 2005; Sánchez-Blázquez et al. 2006; Graves et al. 2007; Smith et al. 2009; Price et al. 2011; Johansson et al. 2012; Conroy et al. 2014; Worthey et al. 2014). One interesting exception is $[\text{N}/\text{Fe}]$, where we see a decline with σ_* . This trend is at odds with our previous finding (Greene et al. 2013), as well as most other work on the topic (although see also Kelson et al. 2006). More detailed work is needed to confirm this trend, particularly given possible uncertainties in flux calibration in the blue for the Mitchell spectra. Recall also that the very old ages found in the very centers of these galaxies have 2–3 Gyr error bars, and thus are consistent with the age of the universe.

Thanks to our spatial coverage, we can go beyond the trends between σ_* and stellar populations in the galaxy center, and look at how these trends evolve as we look to larger radius, both in physical and R_e -scaled units. The crosses in Figure 5 show the trends between σ_* and stellar population properties measured at 3–6 kpc. In general, the same trends are seen with σ_* in the central and 3–6 kpc bins ($[\text{N}/\text{Fe}]$ is again an

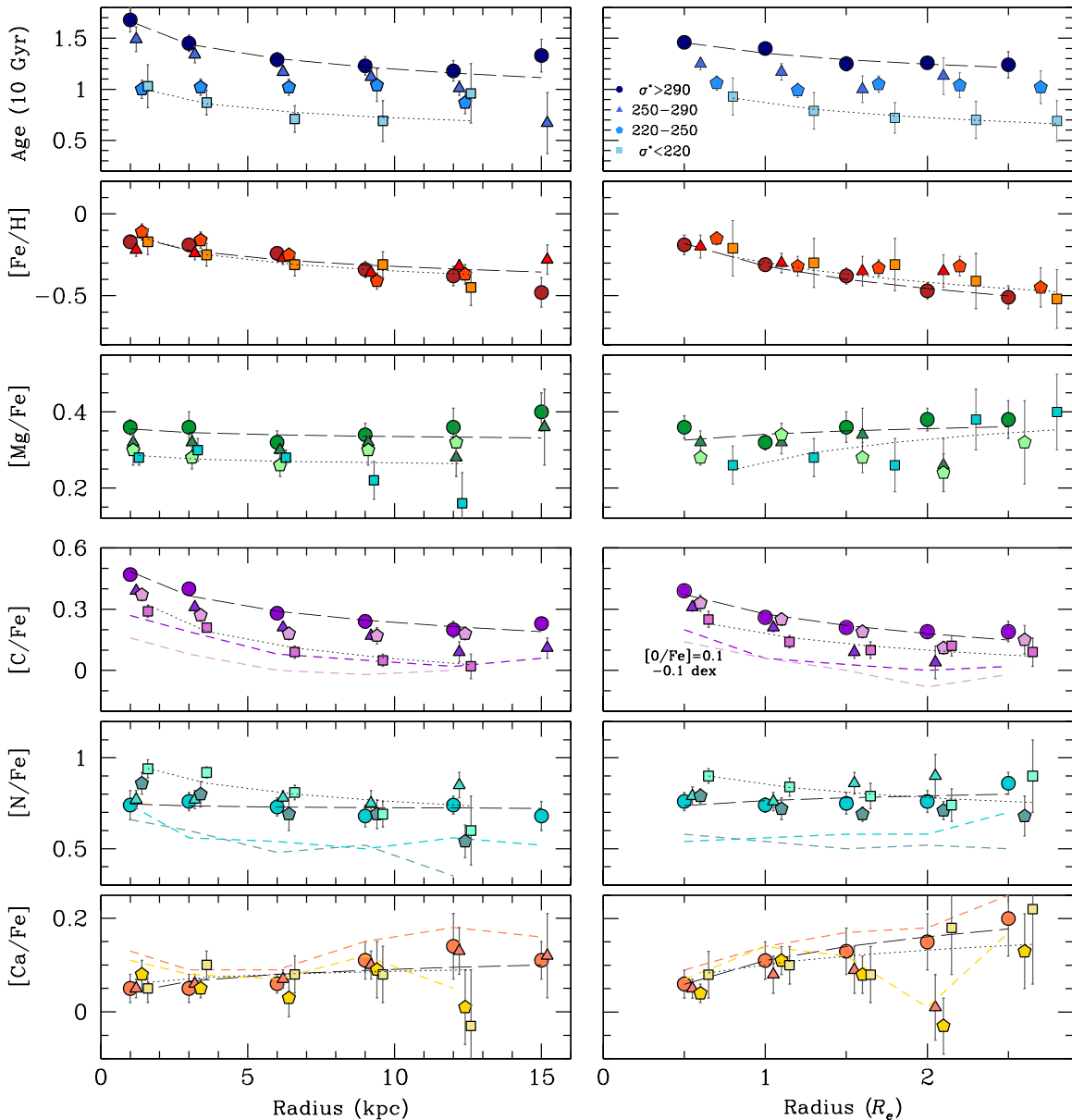


Figure 4. Radial gradients in age, $[\text{Fe}/\text{H}]$, $[\text{Mg}/\text{Fe}]$, $[\text{C}/\text{Fe}]$, $[\text{N}/\text{Fe}]$, and $[\text{Ca}/\text{Fe}]$ as calculated by *EZ_Ages* from the Lick indices measured in the coadded spectra. The measurements are made on four stacked spectra binned on stellar velocity dispersion (see Figure key), and are shown as a function of R in kpc (left) or R/R_e . We fit the radial gradients with a power law of the form $X = A \log(R/R_3) + B$ for each stellar population parameter X , where R_3 is either 3–6 kpc or 1–1.5 R_e . The fits to the highest (long-dashed lines) and lowest dispersion (dotted lines) are shown here, and in Tables 1 and 2. Note the decline with radius in $[\text{Fe}/\text{H}]$ and $[\text{C}/\text{Fe}]$ in contrast with the radially constant age, $[\text{Mg}/\text{Fe}]$, $[\text{N}/\text{Fe}]$, and $[\text{Ca}/\text{Fe}]$. To indicate systematic errors in the light elements due to the unknown oxygen abundance, we also show the resulting models assuming $[\text{O}/\text{Fe}] = 0.1$ rather than the default $[\text{O}/\text{Fe}] = 0.5$ (keeping $[\text{O}/\text{Fe}]$ constant with radius in both cases; $\sigma_* > 290 \text{ km s}^{-1}$ and $220 < \sigma_* < 250 \text{ km s}^{-1}$ are shown in colors that match the symbol). The $[\text{C}/\text{Fe}]$ lines with alternate oxygen abundance have been offset by -0.1 dex for presentation purposes.

exception). Fit values are included in Table 3. $[\text{C}/\text{Fe}]$ shows the most significant correlation with σ_* , with a positive slope detected at 8σ significance. We find a weak trend with $[\alpha/\text{Fe}]$ (3.5σ) and a strong trend with age (7σ ; not shown). The measured slopes between σ_* and $[\text{Fe}/\text{H}]$, $[\text{Ca}/\text{Fe}]$, and $[\text{N}/\text{Fe}]$ are all consistent with zero; that is, the effective value of these parameters is similar for all σ_* bins.

We can also evaluate trends between σ_* and stellar population properties evaluated beyond R_e (taken here to be the 1–1.5 R_e bin). In this case, the physical radii increase for the higher-dispersion bins. Interestingly, we find that the trends with σ_* are weaker when evaluated as a function of R_e . Only stellar age (7σ) and $[\text{C}/\text{Fe}]$ (much more weakly at 4σ) correlate

positively with σ_* . Apparently, trends between σ_* and abundance ratios are strongest when measured within small physical radii. If galaxies indeed form a compact core rapidly at high redshift, then we expect this inner region (< 5 kpc; e.g., van der Wel et al. 2014) to depend most strongly on σ_* .

Before we interpret these observed trends in more detail, we examine differences between bins in σ_* and stellar mass.

5.2. Bins of M^*

There is now a preponderance of evidence that stellar population properties correlate most strongly with σ_* at their centers (Bender et al. 1993; Trager et al. 2000b; Graves et al. 2009; Wake et al. 2012). However, there is little work

Table 1
Gradient Fits (R_c)

Stack	A_{age}	B_{age}	$A_{[\text{Fe}/\text{H}]}$	$B_{[\text{Fe}/\text{H}]}$	$A_{[\alpha]/\text{Fe}}$	$B_{[\alpha]/\text{Fe}}$	$A_{[\text{C}/\text{Fe}]}$	$B_{[\text{C}/\text{Fe}]}$	$A_{[\text{N}/\text{Fe}]}$	$B_{[\text{N}/\text{Fe}]}$	$A_{[\text{Ca}/\text{Fe}]}$	$B_{[\text{Ca}/\text{Fe}]}$
$\sigma_{<220}$	-0.36 ± 0.33	7.41 ± 0.82	-0.39 ± 0.31	-0.37 ± 0.08	0.15 ± 0.12	0.32 ± 0.03	-0.23 ± 0.08	0.12 ± 0.02	-0.21 ± 0.12	0.80 ± 0.04	0.10 ± 0.13	0.12 ± 0.04
$\sigma_{220-250}$	-0.03 ± 0.17	10.2 ± 0.48	-0.34 ± 0.10	-0.32 ± 0.03	0.01 ± 0.06	0.29 ± 0.02	-0.34 ± 0.07	0.18 ± 0.02	-0.16 ± 0.09	0.71 ± 0.03	0.06 ± 0.06	0.08 ± 0.02
$\sigma_{250-290}$	-0.34 ± 0.21	10.8 ± 0.77	-0.28 ± 0.18	-0.34 ± 0.05	-0.04 ± 0.10	0.31 ± 0.03	-0.43 ± 0.07	0.11 ± 0.02	0.13 ± 0.14	0.83 ± 0.04	0.03 ± 0.08	0.07 ± 0.03
$\sigma_{290-400}$	-0.35 ± 0.11	12.9 ± 0.34	-0.46 ± 0.11	-0.40 ± 0.02	0.05 ± 0.06	0.35 ± 0.02	-0.32 ± 0.06	0.22 ± 0.01	0.09 ± 0.10	0.78 ± 0.03	0.17 ± 0.08	0.14 ± 0.03
$M_{K>-24.5}$	-0.37 ± 0.24	9.59 ± 0.56	-0.27 ± 0.11	-0.35 ± 0.03	0.04 ± 0.05	0.34 ± 0.02	-0.33 ± 0.06	0.13 ± 0.01	-0.21 ± 0.10	0.86 ± 0.03	0.02 ± 0.05	0.07 ± 0.02
$M_{K-24.5:-25.5}$	-0.09 ± 0.26	11.3 ± 0.74	-0.44 ± 0.23	-0.32 ± 0.05	-0.04 ± 0.11	0.26 ± 0.03	-0.36 ± 0.06	0.16 ± 0.01	-0.27 ± 0.11	0.76 ± 0.03	-0.01 ± 0.11	0.04 ± 0.02
$M_{K-25.5:-25.8}$	-0.34 ± 0.17	9.01 ± 0.56	-0.37 ± 0.13	-0.30 ± 0.04	0.03 ± 0.08	0.29 ± 0.03	-0.31 ± 0.08	0.17 ± 0.02	-0.03 ± 0.12	0.72 ± 0.04	0.09 ± 0.10	0.09 ± 0.03
$M_{K>-25.8}$	-0.29 ± 0.29	13.0 ± 0.89	-0.54 ± 0.17	-0.52 ± 0.06	0.19 ± 0.08	0.43 ± 0.03	-0.36 ± 0.09	0.20 ± 0.03	0.43 ± 0.12	0.85 ± 0.04	0.10 ± 0.10	0.17 ± 0.03
M_h^*	-0.17 ± 0.21	8.85 ± 0.68	-0.51 ± 0.16	-0.43 ± 0.05	0.19 ± 0.08	0.41 ± 0.03	-0.24 ± 0.07	0.20 ± 0.02	0.16 ± 0.09	0.84 ± 0.02	0.27 ± 0.06	0.14 ± 0.02
M_l^*	-0.24 ± 0.14	8.93 ± 0.38	-0.30 ± 0.08	-0.28 ± 0.02	-0.06 ± 0.04	0.28 ± 0.01	-0.37 ± 0.04	0.17 ± 0.01	-0.23 ± 0.07	0.85 ± 0.02	-0.003 ± 0.03	0.003 ± 0.01
ENV_h	-0.23 ± 0.27	9.78 ± 0.83	-0.44 ± 0.14	-0.42 ± 0.04	0.10 ± 0.08	0.38 ± 0.03	-0.31 ± 0.06	0.19 ± 0.02	0.06 ± 0.10	0.87 ± 0.03	0.19 ± 0.07	0.10 ± 0.02
ENV_l	-0.29 ± 0.14	7.67 ± 0.43	-0.21 ± 0.10	-0.26 ± 0.03	-0.09 ± 0.06	0.27 ± 0.02	-0.38 ± 0.05	0.14 ± 0.01	-0.13 ± 0.11	0.82 ± 0.03	-0.04 ± 0.07	-0.002 ± 0.02
BCG_h	-0.31 ± 0.07	9.40 ± 0.03	-0.40 ± 0.20	-0.41 ± 0.06	0.15 ± 0.07	0.37 ± 0.02	-0.31 ± 0.07	0.18 ± 0.03	0.08 ± 0.12	0.84 ± 0.03	0.19 ± 0.06	0.10 ± 0.02
BCG_l	-0.16 ± 0.18	8.49 ± 0.57	-0.40 ± 0.11	-0.34 ± 0.04	0.06 ± 0.07	0.35 ± 0.02	-0.31 ± 0.07	0.16 ± 0.03	0.04 ± 0.10	0.90 ± 0.02	0.11 ± 0.06	0.06 ± 0.02

Note. Fits to stellar population parameters as a function of radius in units of R_c . For each parameter X , we fit a relation $X = A \log(R/1.5 R_c) + B$. $1.5 R_c$ is the third radial bin, so B represents an effective value for the stellar population property, while A is the radial gradient. These fits are done to stellar population properties derived from bins of (in order from top to bottom) σ_* , M_K , M_K at fixed σ_* , environment or halo mass at fixed σ_* , and then halo mass for only the brightest galaxy in the halo.

Table 2
Gradient Fits (Physical)

Stack	A_{age}	B_{age}	$A_{[\text{Fe}/\text{H}]}$	$B_{[\text{Fe}/\text{H}]}$	$A_{[\alpha/\text{Fe}]}$	$B_{[\alpha/\text{Fe}]}$	$A_{[\text{C}/\text{Fe}]}$	$B_{[\text{C}/\text{Fe}]}$	$A_{[\text{N}/\text{Fe}]}$	$B_{[\text{N}/\text{Fe}]}$	$A_{[\text{Ca}/\text{Fe}]}$	$B_{[\text{Ca}/\text{Fe}]}$
$\sigma_{<220}$	-0.28 ± 0.24	7.75 ± 0.83	-0.20 ± 0.10	-0.31 ± 0.04	-0.02 ± 0.03	0.27 ± 0.02	-0.27 ± 0.04	0.11 ± 0.02	-0.23 ± 0.07	0.81 ± 0.03	0.03 ± 0.05	0.08 ± 0.03
$\sigma_{220-250}$	-0.06 ± 0.12	9.83 ± 0.48	-0.27 ± 0.06	-0.29 ± 0.02	0.00 ± 0.05	0.28 ± 0.02	-0.19 ± 0.04	0.21 ± 0.02	-0.24 ± 0.08	0.69 ± 0.04	-0.04 ± 0.05	0.04 ± 0.02
$\sigma_{250-290}$	-0.42 ± 0.11	11.7 ± 0.34	-0.10 ± 0.04	-0.29 ± 0.02	-0.02 ± 0.03	0.30 ± 0.01	-0.24 ± 0.03	0.21 ± 0.01	0.04 ± 0.07	0.79 ± 0.02	0.05 ± 0.03	0.08 ± 0.01
$\sigma_{290-400}$	-0.47 ± 0.12	13.0 ± 0.43	-0.19 ± 0.05	-0.28 ± 0.02	-0.02 ± 0.03	0.34 ± 0.02	-0.25 ± 0.03	0.29 ± 0.01	-0.02 ± 0.06	0.73 ± 0.02	0.05 ± 0.03	0.08 ± 0.02
$M_{K>-24.5}$	-0.42 ± 0.16	9.78 ± 0.64	-0.20 ± 0.07	-0.36 ± 0.03	-0.02 ± 0.03	0.33 ± 0.02	-0.29 ± 0.04	0.11 ± 0.01	-0.09 ± 0.05	0.88 ± 0.03	0.04 ± 0.03	0.08 ± 0.02
$M_{K-24.5:-25.5}$	-0.11 ± 0.12	11.2 ± 0.58	-0.26 ± 0.15	-0.32 ± 0.05	-0.01 ± 0.08	0.28 ± 0.03	-0.25 ± 0.04	0.20 ± 0.02	-0.19 ± 0.10	0.77 ± 0.04	0.02 ± 0.08	0.05 ± 0.03
$M_{K-25.5:-25.8}$	-0.14 ± 0.13	9.74 ± 0.42	-0.17 ± 0.06	-0.22 ± 0.02	-0.04 ± 0.03	0.28 ± 0.01	-0.25 ± 0.04	0.22 ± 0.01	-0.09 ± 0.06	0.73 ± 0.02	0.03 ± 0.04	0.10 ± 0.02
$M_{K>-25.8}$	-0.76 ± 0.23	13.1 ± 0.49	-0.22 ± 0.12	-0.28 ± 0.03	0.08 ± 0.08	0.35 ± 0.02	-0.27 ± 0.05	0.30 ± 0.01	0.35 ± 0.14	0.70 ± 0.03	0.21 ± 0.10	0.12 ± 0.02
M_h^*	-0.17 ± 0.11	9.06 ± 0.35	-0.15 ± 0.09	-0.26 ± 0.04	0.00 ± 0.04	0.34 ± 0.02	-0.22 ± 0.03	0.26 ± 0.01	-0.10 ± 0.06	0.78 ± 0.02	0.04 ± 0.05	0.06 ± 0.02
M_l^*	-0.24 ± 0.10	9.37 ± 0.39	-0.24 ± 0.04	-0.30 ± 0.02	-0.02 ± 0.02	0.28 ± 0.01	-0.25 ± 0.03	0.18 ± 0.01	-0.14 ± 0.05	0.87 ± 0.03	0.04 ± 0.02	0.03 ± 0.01
ENV_h	-0.27 ± 0.13	10.1 ± 0.46	-0.17 ± 0.09	-0.32 ± 0.04	-0.01 ± 0.04	0.33 ± 0.02	-0.21 ± 0.03	0.25 ± 0.01	-0.05 ± 0.05	0.83 ± 0.02	0.07 ± 0.05	0.06 ± 0.02
ENV_l	-0.07 ± 0.11	8.51 ± 0.38	-0.20 ± 0.06	-0.25 ± 0.02	-0.03 ± 0.03	0.28 ± 0.02	-0.26 ± 0.07	0.15 ± 0.02	-0.15 ± 0.10	0.86 ± 0.04	-0.04 ± 0.08	-0.01 ± 0.03
BCG-h	-0.25 ± 0.04	10.5 ± 0.02	-0.18 ± 0.08	-0.34 ± 0.04	-0.01 ± 0.04	0.33 ± 0.02	-0.20 ± 0.03	0.25 ± 0.01	-0.05 ± 0.07	0.80 ± 0.02	0.04 ± 0.05	0.04 ± 0.02
BCG-l	-0.11 ± 0.09	8.38 ± 0.31	-0.20 ± 0.06	-0.27 ± 0.02	-0.005 ± 0.04	0.33 ± 0.02	-0.21 ± 0.02	0.22 ± 0.02	-0.12 ± 0.06	0.86 ± 0.03	0.01 ± 0.05	0.02 ± 0.02

Note. Fits to stellar population parameters as a function of physical radius. For each parameter X , we fit a relation $X = A \log(R/R_{3-6\text{kpc}}) + B$. $R_{3-6\text{kpc}}$ is the third radial bin, so B represents an effective value for the stellar population property, while A is the radial gradient. These fits are done to stellar population properties derived from bins of (in order from top to bottom) σ_* , M_K , M_K at fixed σ_* , environment or halo mass at fixed σ_* , and then halo mass for only the brightest galaxy in the halo.

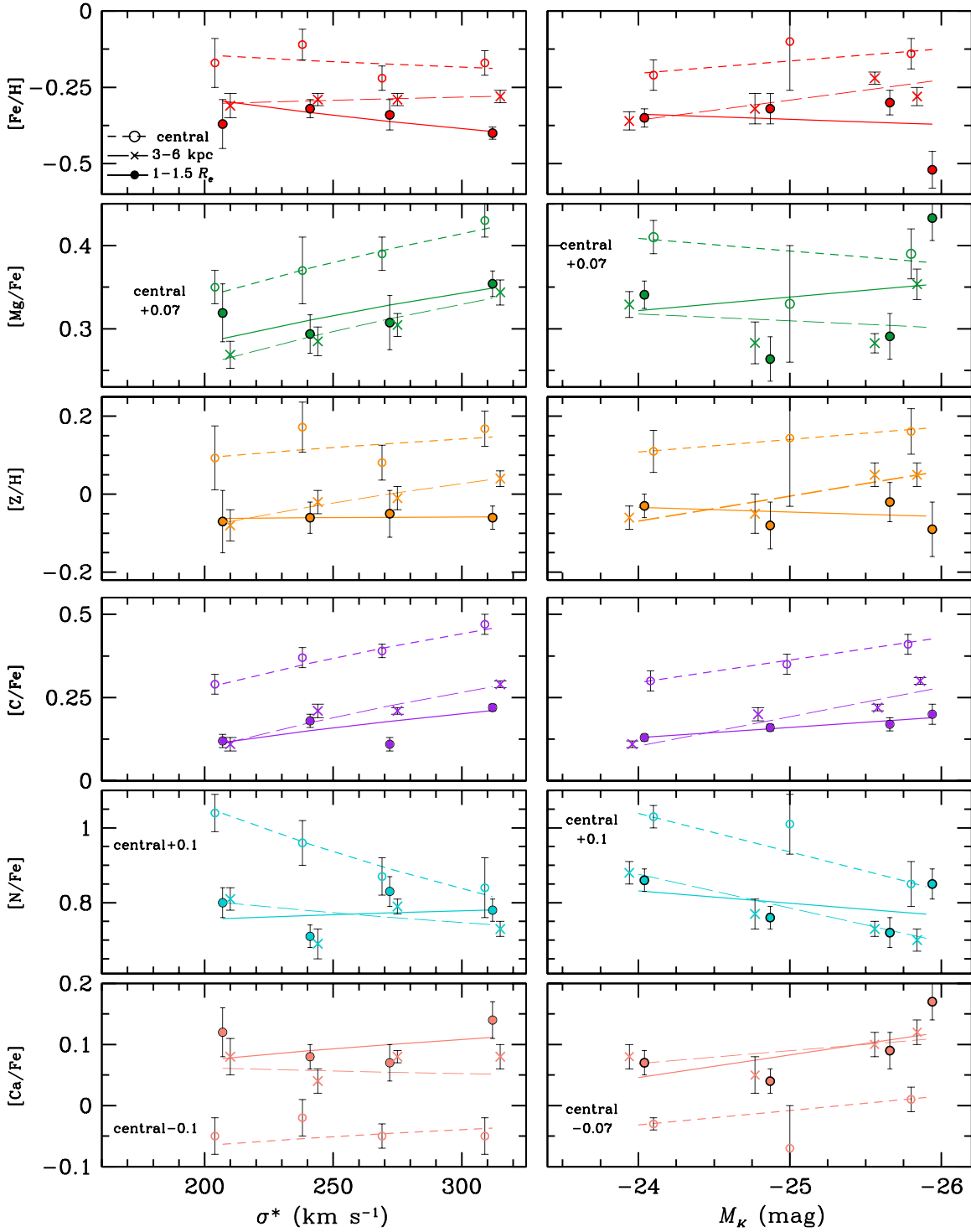


Figure 5. Variation in stellar population parameters X as a function of σ_* (left) and M_K (right). Left: we compare the relation measured from the coadded central fibers (open circles; dashed lines) with those from fits to the profiles weighted to $1-1.5 R_e$ (filled circles; solid lines) and $3-6$ kpc (crosses; long-dashed lines). We plot the fitted zeropoints (B) for each chemical property fitted vs. radius (Tables 1 and 2) as a function of σ_* . $[Z/H]$ is estimated as $[Z/H] = [Fe/H] + 0.94[\alpha/Fe]$, which assumes that $[O/Fe]$ tracks $[Mg/Fe]$. The power-law fits shown here have the form $X = A \log(\sigma_*/250 \text{ km s}^{-1}) + B$ for each stellar population property X (Table 3). We see that the central and $3-6$ kpc fits are generally similar and show the strongest trends with σ_* , while when we scale to R_e the trends are washed out, supporting a scenario where the inner 5 kpc collapsed quickly and scales with the galaxy potential, while the outer parts are accreted from lower-mass systems. Right: as above, but fitting $X = A \log(M_K / -25.3 \text{ mag}) + B$. Note that the central measurement is missing for the highest M_K bin because the $H\beta$ measurement fell off the grid. In general the dispersion in galaxy properties is larger in fixed M_K bins, and the trends weaker. The largest exception is $[C/Fe]$ which shows a stronger correlation with M_K than σ_* .

comparing radial trends as a function of mass and σ_* (Spolaor et al. 2010). We therefore create four bins of K -band magnitude, based on 2MASS photometry (Jarrett et al. 2003; Skrutskie et al. 2006): $M_K > -24.5$ (21 galaxies), $-24.5 > M_K > -25.5$

(23), $-25.5 > M_K > -25.8$ (24), and $M_K < -25.8$ mag (19; Figure 6). We note that there is a wide range of stellar velocity dispersion at each mass bin (Figure 1), so this binning scheme is truly different from the dispersion bins presented above.

Table 3
Galaxy Correlations at Varying Radii

Radius	$A_{[\text{Fe}/\text{H}]}$	$B_{[\text{Fe}/\text{H}]}$	$A_{[\text{Z}/\text{H}]}$	$B_{[\text{Z}/\text{H}]}$	$A_{[\alpha/\text{Fe}]}$	$B_{[\alpha/\text{Fe}]}$	$A_{[\text{C}/\text{Fe}]}$	$B_{[\text{C}/\text{Fe}]}$	$A_{[\text{N}/\text{Fe}]}$	$B_{[\text{N}/\text{Fe}]}$	$A_{[\text{Ca}/\text{Fe}]}$	$B_{[\text{Ca}/\text{Fe}]}$
σ^* Fit												
Center	-0.23 ± 0.43	-0.17 ± 0.03	0.28 ± 0.47	0.12 ± 0.03	0.44 ± 0.15	0.31 ± 0.01	0.93 ± 0.22	0.37 ± 0.01	-1.25 ± 0.46	0.83 ± 0.03	-0.05 ± 0.22	0.06 ± 0.01
1–1.5 R_e	-0.56 ± 0.28	-0.34 ± 0.02	0.02 ± 0.36	-0.06 ± 0.03	0.34 ± 0.18	0.32 ± 0.01	0.54 ± 0.11	0.16 ± 0.01	0.13 ± 0.26	0.77 ± 0.02	0.19 ± 0.25	0.09 ± 0.01
3–6 kpc	0.13 ± 0.20	-0.29 ± 0.01	0.63 ± 0.22	-0.02 ± 0.02	0.41 ± 0.12	0.30 ± 0.01	0.96 ± 0.11	0.19 ± 0.01	-0.33 ± 0.20	0.77 ± 0.01	0.15 ± 0.18	0.07 ± 0.01
M_K Fit												
Center	-0.04 ± 0.04	-0.15 ± 0.04	-0.03 ± 0.05	0.15 ± 0.05	0.01 ± 0.02	0.32 ± 0.02	-0.07 ± 0.03	0.38 ± 0.02	0.10 ± 0.04	0.80 ± 0.04	-0.02 ± 0.01	0.07 ± 0.02
1–1.5 R_e	0.02 ± 0.03	-0.36 ± 0.02	0.01 ± 0.03	-0.05 ± 0.03	-0.02 ± 0.01	0.34 ± 0.01	-0.03 ± 0.01	0.17 ± 0.01	0.03 ± 0.02	0.79 ± 0.02	-0.04 ± 0.02	0.09 ± 0.01
3–6 kpc	-0.07 ± 0.02	-0.27 ± 0.01	-0.06 ± 0.02	0.01 ± 0.02	0.01 ± 0.01	0.31 ± 0.01	-0.09 ± 0.01	0.22 ± 0.01	0.09 ± 0.02	0.76 ± 0.01	-0.02 ± 0.01	0.10 ± 0.01

Note. Fits to stellar population parameters as a function of σ^* or M_K , weighted to different radii. For each stellar population parameter X , we fit a relation $X = A \log(\sigma^*/250 \text{ km s}^{-1}) + B$ (top) and $X = A \log(M_K / -25.3 \text{ mag}) + B$ (bottom). X comes from the central binned data, from the fit in Table 1 weighted to 1–1.5 R_e , and finally from the fits in Table 2, weighted to 3–6 kpc.

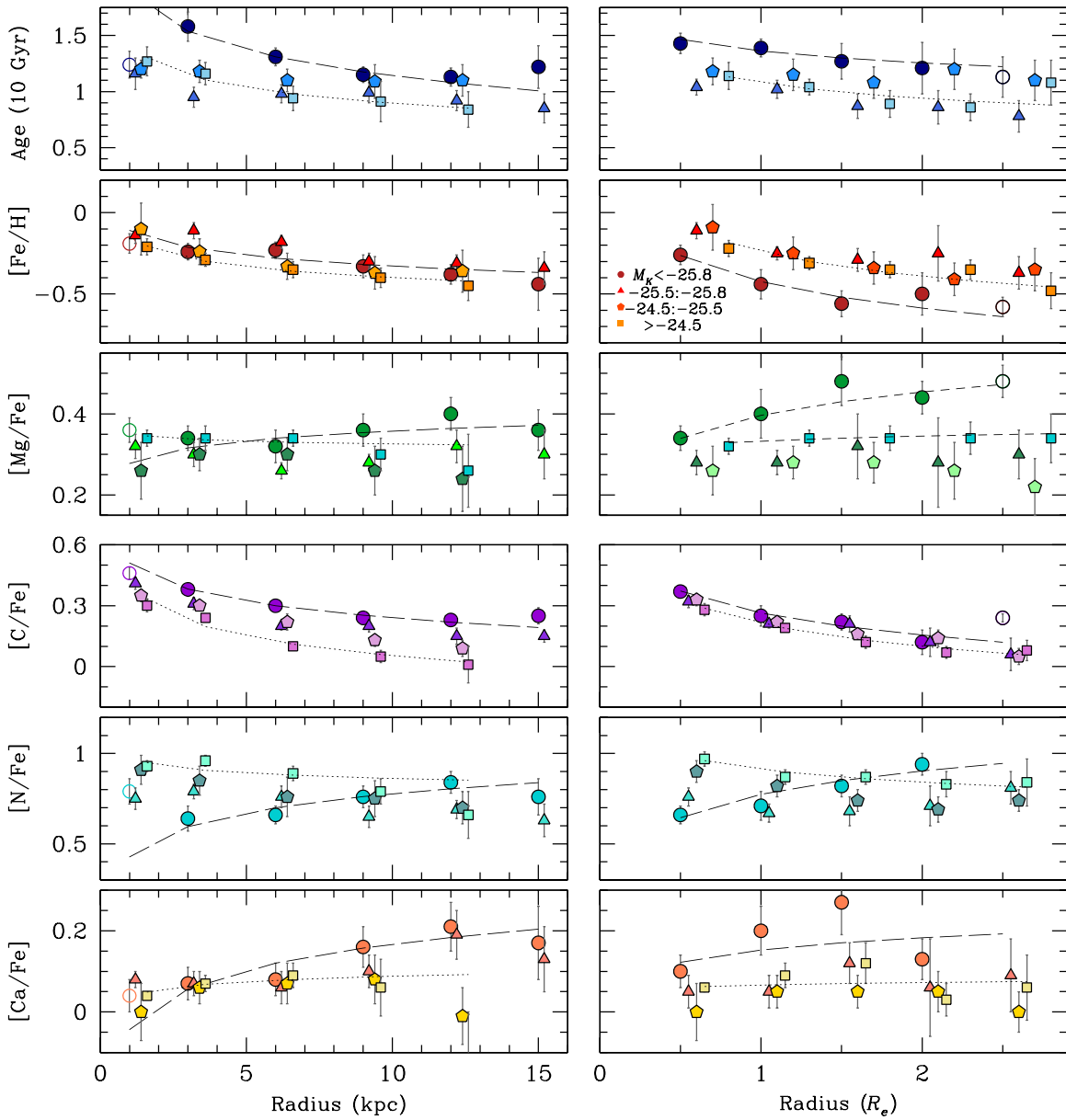


Figure 6. Radial gradients in age, $[\text{Fe}/\text{H}]$, $[\text{Mg}/\text{Fe}]$, $[\text{C}/\text{Fe}]$, $[\text{N}/\text{Fe}]$, and $[\text{Ca}/\text{Fe}]$ as above, but now in bins of M_K (mag; a proxy for stellar mass) rather than stellar velocity dispersion. Open symbols indicate cases where the primary measurement fell off the stellar population grid and we have used the median of the distribution of boot-strap stacks instead. The inversion program failed to converge for the $[\text{N}/\text{Fe}]$ and $[\text{Ca}/\text{Fe}]$ measurements for the outermost high- M_K R_e -scaled point, so no measurement is shown. As indicated in the key, the bins have $M_K > -24.5$ (squares), $-24.5 > M_K > -25.5$ (pentagons), $-25.5 > M_K > -25.8$ (triangles), and $M_K < -25.8$ mag (circles) respectively. We fit the radial gradients with a power law of the form $X = A \log(R/R_3) + B$ for each stellar population parameter X , where R_3 is either 3–6 kpc or 1–1.5 R_e . Fits to the most massive (long-dashed lines) and least massive (dotted lines) galaxies are shown here; all fitted coefficients are in Tables 1 and 2.

As above, we fit each stellar population property as a function of radius, tabulated in Tables 1 and 2. Each effective stellar population parameter is shown as a function of M_K in Figure 5 (right). Starting as in Section 5.1 by focusing on the central measurements, we see that in general, there is more dispersion in stellar population properties (particularly metallicity and $[\text{Mg}/\text{Fe}]$) in a given M_K bin as compared with a given σ_* bin. In particular, the second M_K bin (-24.5 to -25.5 mag) shows considerably larger variance than the other bins. We believe that this larger error bar reflects a genuine increase in the spread in stellar populations in this bin. At yet lower M_K , we no longer have a representative sample of objects. We also generally see weaker trends in the stellar populations with M_K than with σ_* , particularly in physically scaled bins (Table 3).

The exception is $[\text{C}/\text{Fe}]$, which shows a more significant correlation with M_K (12σ). We see no correlation with age or $[\alpha/\text{Fe}]$. There is, however, a marginal correlation with $[\text{Fe}/\text{H}]$ (3σ) and a corresponding weak correlation with $[\text{Z}/\text{H}]$ (also 3σ). If we instead consider measurements from 1.5 R_e , we find no significant trends between stellar population properties and M_K (not even stellar age).

5.2.1. Bins in M^* at Fixed σ_*

We now ask whether, at fixed σ_* , there are residual trends in the stellar population gradients as a function of stellar mass (Figure 7). We create two luminosity bins divided at $M_K = -25$ mag (which approximately divides the sample in

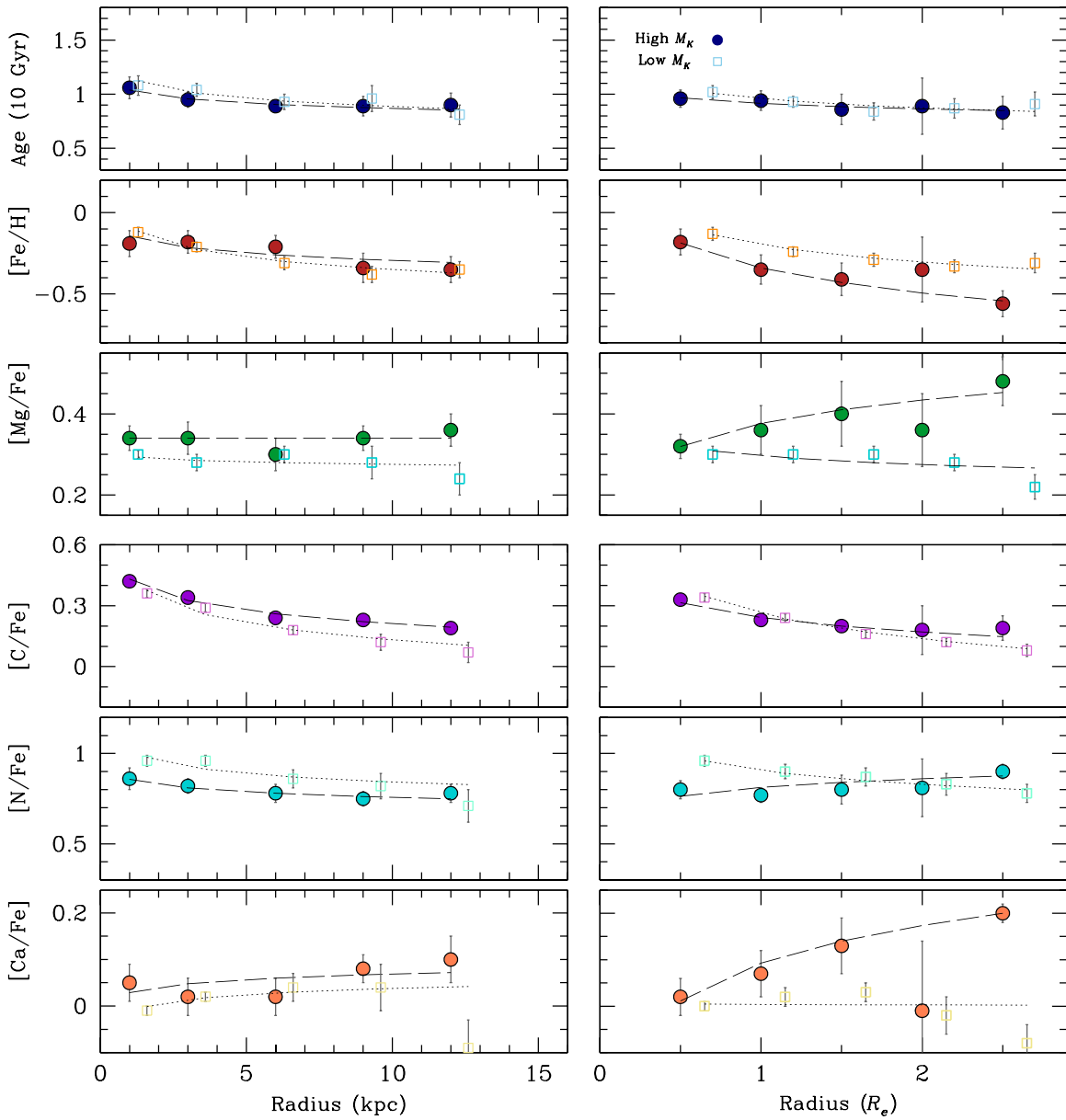


Figure 7. Radial gradients in age, [Fe/H], [Mg/Fe], [C/Fe], [N/Fe], and [Ca/Fe] as above, but now in σ_* -matched bins of M_K (mag; a proxy for stellar mass). Filled symbols have $M_K < -25$ mag while open symbols have $M_K > -25$ mag. We fit the radial gradients with a power law of the form $X = A \log(R/R_3) + B$ for each stellar population parameter X , where R_3 is either 3–6 kpc or 1–1.5 R_e . The fits to the high-mass (long-dashed lines) and low-mass (dotted lines) bins are shown here and in Tables 1 and 2.

two). We then enforce a matched distribution in σ_* between 200 and 330 km s^{-1} by creating 100 stacks for each mass bin, each having an identical distribution of σ_* and each including a total of 30 galaxies.

We find small but detectable differences in the two mass bins. Specifically, while the average stellar population ages are both ~ 9.5 Gyr, we find that the high-mass bin is more α -enhanced by ~ 0.1 dex with (possibly) correspondingly lower [Fe/H] at fixed R_e (Table 1). The C and N abundances and radial profiles are consistent with each other, but there is a hint that the more massive galaxies are also more Ca-enhanced at fixed σ_* . All of these trends could be qualitatively explained if the timescale for star formation were shorter in the more massive systems, such that [Fe/H] is lower while $[\alpha/\text{Fe}]$ is higher and [Ca/H] follows [Fe/H].

The other possible explanation is that at fixed σ_* , more massive galaxies are physically larger. This would explain why at a fixed fraction of R_e , the more massive galaxies have lower [Fe/H]. Graves et al. (2009) find that galaxies with the lowest central surface brightness also have the oldest ages and lowest [Fe/H] values, a similar trend to that seen here, albeit only for galaxy centers. When we have robust size measurements for our sample galaxies we will revisit the question of stellar populations through the Fundamental Plane, also including radial stellar population information.

5.3. Interpreting Stellar Populations Using Radial Trends

There are a number of interesting trends seen in the stellar populations of elliptical galaxy centers that challenge our understanding, particularly when compared with Galactic

trends. It is our hope that adding radial information will shed new light not only on the assembly history of ellipticals, but also on the nucleosynthetic yields that lead to these observed trends.

There are a few important caveats to keep in mind as we interpret the observations. First, our stellar ages, particularly at the center, are subject to large ($\sim 2\text{--}3$ Gyr) uncertainties. Thus, we caution against over-interpreting the radial trends in age at present. Some work covering larger dynamic range in radius do detect clear age gradients (e.g., La Barbera et al. 2012), but we do not go to large enough radius to detect the very low metallicity true halo component that has been seen in a few nearby cases (e.g., Harris et al. 2007; Williams et al. 2015). Second, we remain cautious about the nitrogen measurements given the possible flux calibration difficulties at the blue end of the spectrum. Third, recall that we are examining average trends in stacked spectra. Undoubtedly there are interesting exceptions to all of these trends, and we plan to study the full range of parameters in future work.

We revisit our expectations for stellar population trends as a function of radius in light of the recent picture that galaxies form in two “phases,” an initial burst of in situ star formation creating the central component, followed by late-time accretion of smaller, fluffier units at larger radius (e.g., Naab et al. 2009). For galaxies in our mass range, the typical sizes of the central components are measured to be 2–5 kpc at $z \approx 2$ (e.g., van der Wel et al. 2014). When we look at the stellar populations at this typical radius (Figure 5), we find that age and $[\alpha/\text{Fe}]$ depend on σ_* rather than M_K . Since we expect galaxies that form early to be denser and have higher σ_* , a stronger correlation between age and star formation timescale with σ_* seems natural. In contrast, $[\text{Fe}/\text{H}]$, $[\text{C}/\text{Fe}]$, and $[\text{N}/\text{Fe}]$ depend more on the total stellar mass of the system.

In addition to considering a fixed physical radius, we look at stellar population trends at $\sim 1.5 R_e$ (Figure 5). According to simulations, more massive galaxies are increasingly dominated by accreted stars at radii beyond ~ 5 kpc (e.g., Oser et al. 2010). Therefore we might expect the correlation between σ_* and stellar population properties to decrease when taken over the bulk of the stellar population. This is what we observe. Beyond $\sim R_e$ we find no strong trend between σ_* or M_K and abundances or abundance ratios. This result builds on what we saw in Greene et al. (2013). There, we emphasized that the stellar populations beyond R_e in massive galaxies tend to have low $[\text{Fe}/\text{H}] \sim -0.5$ dex and high $[\alpha/\text{Fe}] \sim 0.3$ dex, stellar populations that are not seen in the centers of any galaxies today (see also Bender et al. 2015). Here we see that beyond R_e , galaxies over a relatively wide range in σ_* and M_K have similar abundances and abundance ratios, as expected if the more massive galaxies were built by accreting the less massive. Only stellar age is still seen to increase at higher σ_* when examined at $\sim R_e$; we await better age measurements to verify this result.

Another ongoing discussion in the literature regards carbon. As is seen here, $[\text{C}/\text{Fe}]$ is observed to increase with σ_* in elliptical galaxy centers (e.g., Trager et al. 1998; Graves et al. 2007; Johansson et al. 2012; Conroy et al. 2014). This is in contrast to the behavior of carbon in the Milky Way or Local Group dwarf galaxies (e.g., Kirby et al. 2015). To get such super-solar carbon levels in the short timescales implied by the high ratio of $[\alpha/\text{Fe}]$, carbon must come not only from intermediate-mass (AGB) stars but also from massive stars

(Graves et al. 2007; Tang et al. 2014). Carbon yields from massive stars are thought to increase with increasing metallicity due to increased mass-loss from winds (e.g., Maeder 1992). These same high yields at high metallicity are also invoked to explain abundance trends in Milky Way stars (e.g., Henry et al. 2000). If true, we would expect that as the metallicity decreases outwards in these elliptical galaxies, the $[\text{C}/\text{Fe}]$ would also decrease. This is what we observe (Greene et al. 2013). Interestingly, we find that the $[\text{C}/\text{Fe}]$ gradient follows the decline in $[\text{Fe}/\text{H}]$ in both the σ_* and M_K bins.

There is also considerable debate in the literature about the origin and behavior of nitrogen in elliptical galaxy centers (e.g., Kelson et al. 2006; Johansson et al. 2012). Our surprising results are two-fold. First, $[\text{N}/\text{Fe}]$ is remarkably super-solar. Even assuming solar $[\text{O}/\text{Fe}]$ (at odds with the observed $[\text{Mg}/\text{Fe}]$) $[\text{N}/\text{Fe}]$ is found to be three times the solar value. Second, since the N is produced by C through the CNO cycle, their different behavior with radius is non-intuitive (and may point to a changing O abundance as well). As discussed above, the flux calibration at the blue end of the spectrum, containing CN, is quite uncertain. We do find good agreement between CN as measured from the SDSS spectra and the central Mitchell fiber. We also confirm that the CN measurements do not depend on how we treat the continuum. Including or excluding the overall continuum level in the stacks changes the CN1 measurement by <0.005 mag, resulting in very small <0.02 dex in the $[\text{N}/\text{Fe}]$ ratio. To really confirm these high N abundance ratios at large radius, we would like to perform full spectral modeling to mitigate the impacts of blending and the uncertainties introduced by oxygen. In the meantime, it is interesting to note other stellar systems that display very super-solar nitrogen abundance ratios. For instance, in globular clusters, the wide range in $[\text{N}/\text{Fe}]$ strongly suggests pre-enrichment by a previous early epoch of star formation (e.g., Cohen et al. 2005).

Finally, we come to Ca. While nominally an α -element, it has long been known, based on both Ca4227 in the blue and the calcium triplet (CaT) index in the red, that Ca is under-abundant with respect to the other α elements (e.g., Cohen 1979; Terlevich et al. 1990; Vazdekis et al. 1997; Worthey 1998; Peletier et al. 1999; Proctor & Sansom 2002; Saglia et al. 2002; Thomas et al. 2003; Choi et al. 2014). Like $[\text{Fe}/\text{H}]$, $[\text{Ca}/\text{Fe}]$ shows no dependence on σ_* . There are a number of explanations in the literature for the CaT measurements, including changes in the initial mass function (e.g., Cenarro et al. 2004) or a minority metal-poor population (Saglia et al. 2002). However, to explain both the blue and red index behavior, it is more natural to presume that Ca behaves like an Fe-peak element because it is predominantly produced in SNe Ia (e.g., Worthey 1998; Worthey et al. 2011; Conroy et al. 2014). As expected in that case, we measure a flat $[\text{Ca}/\text{Fe}]$ ratio with radius. The one intriguing difference is the possible increase in $[\text{Ca}/\text{Fe}]$ at large radius, which is worth pursuing.

5.4. Bins of Group Richness

While there are well-documented differences in the morphological mix of galaxies as a function of local galaxy density (Dressler 1980), the observations of environmental differences in stellar population properties are quite subtle (e.g., Thomas et al. 2005; Zhu et al. 2010; Lackner & Gunn 2013). Early studies found evidence for younger ages in “field” galaxies (e.g., Terlevich & Forbes 2002). A number of other studies

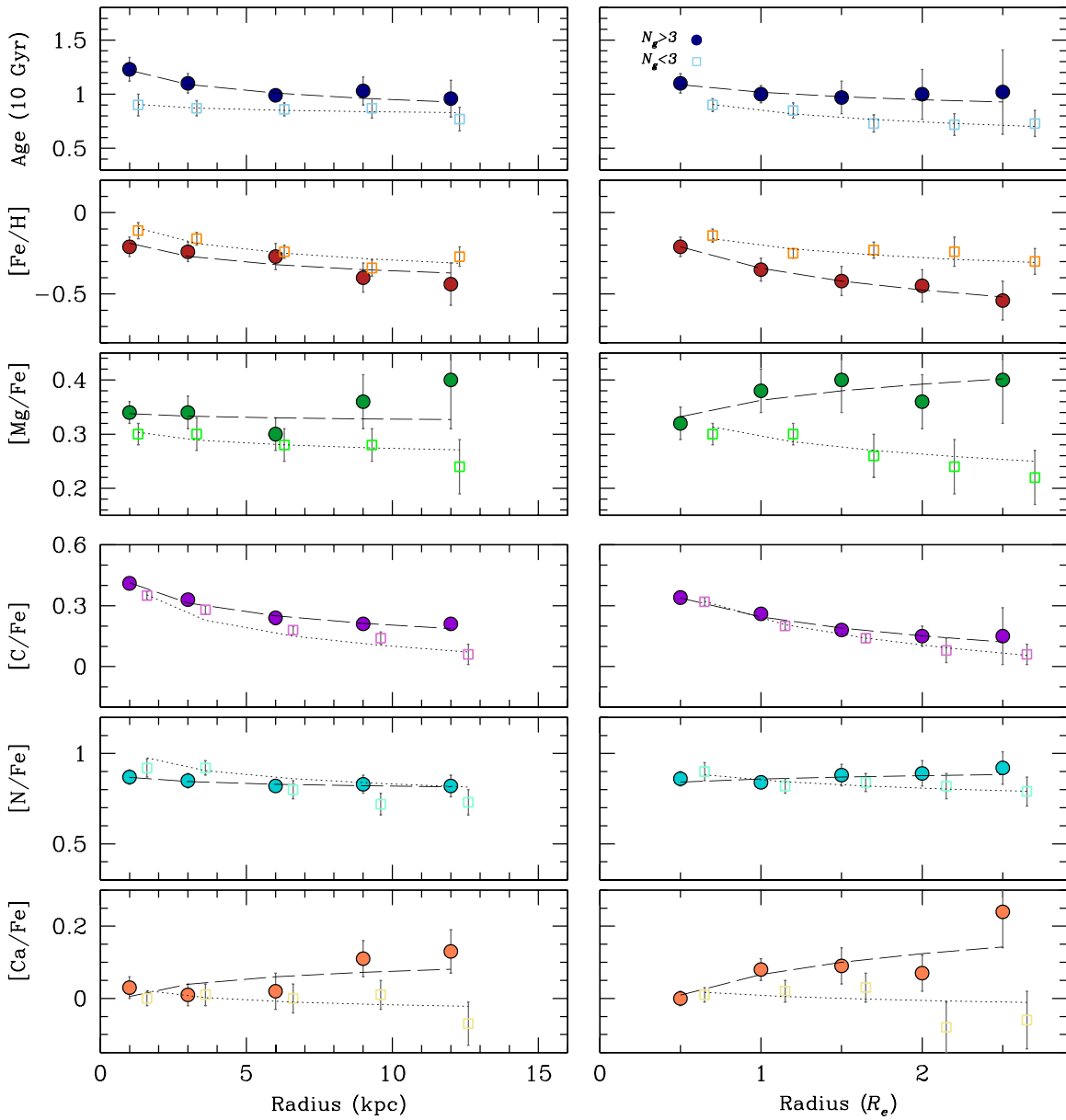


Figure 8. Radial gradients in age, [Fe/H], [Mg/Fe], [C/Fe], [N/Fe], and [Ca/Fe] as above, but now in bins of group richness, controlling for the distribution of σ_* . Low density (open squares) have three or fewer neighbors with $L > L^*$, while filled circles include everything else. We fit the radial gradients with a power law of the form $X = A \log(R/R_3) + B$ for each stellar population parameter X , where R_3 is either 3–6 kpc or $1\text{--}1.5 R_e$. The fits to the rich (long-dashed lines) and poor (dotted lines) bins are shown here and in Tables 1 and 2.

report no change in scaling relations between stellar population parameters and σ_* as a function of local environment (e.g., Kuntschner et al. 2002; Bernardi et al. 2006), but do find a larger fraction of “rejuvenated” galaxies with recent star formation in low-density environments (e.g., Annibali et al. 2007; Thomas et al. 2010). Recently, the samples have grown large enough to evaluate not just the average properties of field and cluster galaxies, but to control for stellar and halo mass (e.g., Pasquali et al. 2010). For instance, Pasquali et al. find that satellite galaxies at fixed mass grow older and more metal-rich as their host halo mass increases.

There is precious little literature on radial gradients in stellar populations as a function of group richness, although a few photometric studies find steeper metallicity gradients in lower-density environments (Ko & Im 2005; La Barbera et al. 2005). Given our large sample and wide range of measured group

richness (Ma et al. 2014), we are in a unique position to examine radial stellar population trends with environment.

To divide the sample by richness, we use the group catalog of Crook et al. (2007). When we divide our galaxies based on group richness alone, the distributions in σ_* do not match. Instead, there are more high σ_* galaxies in richer groups. Since σ_* is strongly correlated with stellar population properties, we must match the σ_* distributions across different halo mass bins. Therefore, we divide the sample in half based on the number of neighbors: “low” comprises galaxies with no more than three companions of $>L^*$ while “high” comprises the rest. The raw distribution of σ_* have median $\langle\sigma_*\rangle = 240 \text{ km s}^{-1}$ for the low-density bin and $\langle\sigma_*\rangle = 260 \text{ km s}^{-1}$ for the high-density bin. Since there are not sufficient numbers to further subdivide the galaxies into bins of σ_* , we create 100 stacks, drawing from the objects with σ_* between 200 and 330 km s^{-1} . We force the low-

density and high-density stacks to have the same number of objects (24 in this case) with the same distribution of σ_* . We do not have sufficient numbers to match on M_k as well; two-thirds of the rich galaxies are also in the brighter half of the sample. The results are shown in Figure 8.

There are only very slight differences between the two galaxy samples divided by group richness. The high-density stack is slightly older, has slightly lower [Fe/H], and slightly higher $[\alpha/\text{Fe}]$, similar to some previous studies (e.g., Bernardi et al. 2006; Clemens et al. 2009; Cooper et al. 2010). The basic interpretation is that objects found in the highest density peaks today likely formed earlier, and thus have older ages, higher $[\alpha/\text{Fe}]$, and slightly lower [Fe/H] (although they maintain roughly solar metallicity overall). Again, the other possibility is that at fixed σ_* , galaxies in denser environments tend to be slightly larger. We plan to control for galaxy size in future work. Turning to the other light elements, we find that [C/Fe] is marginally higher in the high-density bin, while [N/Fe] and [Ca/Fe] are comparable between the two. Finally, it is interesting to note that the sample variance is larger for the low-density sample.

We see marginal evidence for a steeper [Fe/H] gradient in the higher halo-mass bin as a function of effective radius (Figure 8, right; -0.44 ± 0.14 for the higher halo mass bin, -0.2 ± 0.1 for the lower halo mass bin). The slope difference is only significant at $\sim 2\sigma$. $[\alpha/\text{Fe}]$ also shows a very marginal difference in the opposite direction, with slopes of 0.1 ± 0.08 and -0.09 ± 0.06 for the higher and lower halo mass bins respectively. Because of the anti-correlation between [Fe/H] and $[\alpha/\text{Fe}]$, the resulting gradients in [Z/H] for the two bins are comparable (-0.3 ± 0.1 in both cases). If this result is confirmed, it perhaps suggests that at a given σ_* , galaxies in richer environments are more compact, and thus show steeper [Fe/H] gradients. While we do see marginal differences between [Fe/H] and $[\alpha/\text{Fe}]$, we do not confirm results from previous photometric surveys that reported steeper metallicity gradients in lower density environments (Ko & Im 2005; La Barbera et al. 2005).

la Barbera et al. (2014) argue that in addition to looking for trends as a function of halo mass, we should also be dividing the samples into “central” (the most massive galaxy in a halo) and “satellite” galaxies. We therefore repeat the stacking exercise, but this time removing all satellite galaxies (Figure 9); we do not have sufficient numbers of satellite galaxies to stack them alone. Interestingly, when we examine central galaxies alone, the marginal stellar population differences discussed above vanish (although we note that our statistical power is lessened by the smaller sample size as well). Perhaps the differences between the two samples are driven by differing fractions of satellite galaxies in the two environmental stacks, but better statistics are needed before we can be sure. On the other hand, studies of individual brightest cluster galaxies in rich clusters find a wide spread in central properties such as age and $[\alpha/\text{Fe}]$ (e.g., Oliva-Altamirano et al. 2015), as well as evidence for distinct accretion episodes (e.g., Coccato et al. 2010, 2011). In future work we will investigate in more detail the spread in central galaxy properties as a function of halo mass.

We do not reproduce the trend found by La Barbera et al. that the central galaxies are younger in the larger halos. Instead, when we focus on central galaxies only, we see no significant difference between the stellar populations of the two groups at the 0.1 dex level. On the other hand, “low-mass” halos in the

La Barbera study have $M_h < 10^{12.5} M_\odot$. This is considerably lower than the likely halo mass of our galaxies, given that their stellar masses reach $M^* \approx 10^{12} M_\odot$. Furthermore, the differences reported by La Barbera et al. are at the 0.025 dex level, not yet accessible with our data.

6. SUMMARY

Using integral-field spectroscopy, we have looked at the average stellar population gradients for a large sample of 100 early-type massive galaxies. We are able to reach radii $\sim 2.5 R_e$ or ~ 15 kpc. In keeping with previous results, we find no significant gradients in stellar population age nor $[\alpha/\text{Fe}]$ abundance ratios with radius, and gentle gradients in [Fe/H]. We thus confirm our previous result that the stellar populations in the outskirts of massive galaxies have sub-solar [Fe/H] but are enhanced in $[\alpha/\text{Fe}]$, suggesting that the stars formed quickly and early, but in shallow potentials (Greene et al. 2013; Bender et al. 2015).

We examine the stellar population properties weighted toward 3–6 kpc, the typical sizes of massive galaxy cores as observed at $z \approx 2$ (e.g., van der Wel et al. 2014). We see that age and $[\alpha/\text{Fe}]$ rise with increasing σ_* , as we might expect if denser galaxies with higher σ_* form earlier. We also find that at fixed physical radius, [Fe/H] and [C/Fe] correlate more strongly with M_K than stellar velocity dispersion. In contrast, when looking at bins weighted toward $\sim R_e$, we find no strong trends between abundances or abundance ratios and σ_* or M_K . The average star as measured near the half-light radius in the most massive ellipticals is similar to the average star as measured at the half-light radius in galaxies of lower mass, as we might expect if large galaxies grow via accreting smaller satellites. We do, however, still see a trend between stellar age and σ_* even in the R_e -weighted bins.

The gradients in [C/Fe] are similar to those seen in [Fe/H]. We suggest that the C comes mainly from mass loss in massive stars because there is not time to get it from intermediate-mass AGB stars (e.g., Graves et al. 2007). Higher yields due to mass loss from metal-rich stars (e.g., Maeder 1992) cause a pseudo-secondary dependence of carbon on Fe. In contrast, we see super-solar [N/Fe] that persists to large radius; the mismatch between [C/Fe] and [N/Fe] is a puzzle. [Ca/Fe] has solar values over the entire radial range that we observe (with the possible exception of a rise at large radius in the high dispersion bin), consistent with the idea that significant Ca is produced in SNe Ia.

Thanks to our relatively large sample, we are able to examine trends in stellar mass at fixed σ_* . At fixed σ_* , we find marginal evidence that galaxies with higher stellar mass are more α -enhanced and [Ca/Fe] enhanced (because they are slightly [Fe/H] poor), suggesting a shorter timescale for star formation in more massive systems.

Finally, we perform one of the most extensive spectroscopic studies of stellar population gradients as a function of group richness, while controlling for σ_* . Overall, the differences in stellar population properties at large radius as a function of richness are very small, suggesting that internal properties like σ_* determine stellar population gradients (as in galaxy centers; e.g., Zhu et al. 2010). Galaxies in richer environments ($N_{\text{nei}} > 3$) tend to be slightly older, slightly α -enhanced, and slightly [Fe/H] poor. We also see very slight trends toward shallower declines in [Fe/H] in lower-mass halos. When we restrict attention to only central galaxies, these slight

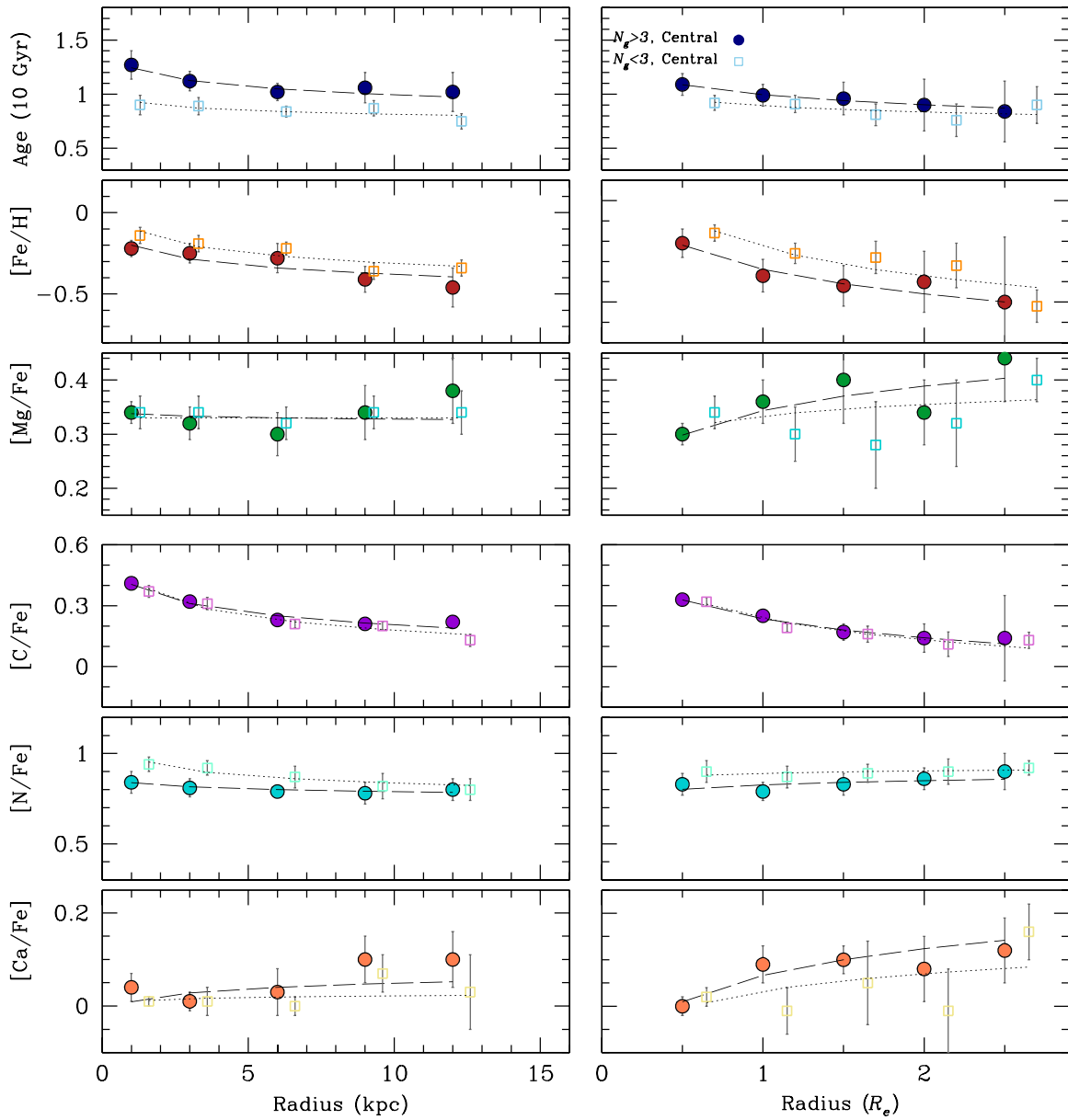


Figure 9. Radial gradients in age, [Fe/H], [Mg/Fe], [C/Fe], [N/Fe], and [Ca/Fe] as above, but now in bins of group richness for so-called central galaxies (the most massive galaxy in the group, according to the Crook et al. 2007 catalog). As above, we divide the sample into those with three or fewer neighbors, and all the rest. We also control the distribution in σ_* to match between the two bins. We fit the radial gradients with a power law of the form $X = A \log(R/R_3) + B$ for each stellar population parameter X , where R_3 is either 3–6 kpc or 1–1.5 R_e . The fits to the rich (long-dashed lines) and poor (dotted lines) bins are shown here and in Tables 1 and 2.

differences vanish, perhaps suggesting that they are driven by the fraction of satellite galaxies in the stacks. These trends are quite weak. Better statistics are needed to confirm them. Furthermore, it will be quite interesting to combine our dynamical and stellar population information (e.g., Jimmy et al. 2013; Naab et al. 2014; Raskutti et al. 2014).

By the end of the MASSIVE survey, we should roughly double the number of $M_K < -25.3$ mag galaxies in the sample, improving our ability to examine trends with environment and mass at fixed σ_* . Our sample will be further complemented by ongoing ambitious integral-field galaxy surveys such as CALIFA (Sánchez et al. 2012), MaNGA (Bundy et al. 2015), and SAMI (Croom et al. 2012). When combined with our dynamical constraints on the total masses of these galaxies, these stellar population constraints on the age and the

mass-to-light ratios of the galaxies will help address a number of pressing questions in galaxy evolution, including the dependence of the initial mass function of σ_* , the ratio of black hole mass to stellar mass at the high mass end, and the role of dark matter halo mass in the internal evolution of massive galaxies.

We thank the referee for a prompt and helpful report. C.P.M. and J.E.G. acknowledge funding from N.S.F. grants AST-1411945 and AST-1411642. N.J.M. is supported by the Beatrice Watson Parent Fellowship. J.E.G. gratefully acknowledges conversations with J.E. Gunn and R. Schiavon. This research has made use of the NASA/IPAC Extragalactic Database (NED) which is operated by the Jet Propulsion Laboratory, California Institute of Technology, under contract

with the National Aeronautics and Space Administration. The Pan-STARRS1 Surveys (PS1) have been made possible through contributions of the Institute for Astronomy, the University of Hawaii, the Pan-STARRS Project Office, the Max-Planck Society and its participating institutes, the Max Planck Institute for Astronomy, Heidelberg and the Max Planck Institute for Extraterrestrial Physics, Garching, The Johns Hopkins University, Durham University, the University of Edinburgh, Queens University Belfast, the Harvard-Smithsonian Center for Astrophysics, the Las Cumbres Observatory Global Telescope Network Incorporated, the National Central University of Taiwan, the Space Telescope Science Institute, the National Aeronautics and Space Administration under grant No. NNX08AR22G issued through the Planetary Science Division of the NASA Science Mission Directorate, the National Science Foundation under grant No. AST-1238877, the University of Maryland, and Eotvos Lorand University (ELTE). We thank the PS1 Builders and PS1 operations staff for construction and operation of the PS1 system and access to the data products provided.

REFERENCES

- Adams, J. J., Gebhardt, K., Blanc, G. A., et al. 2012, *ApJ*, **745**, 92
- Adams, J. J., Blanc, G. A., Hill, G. J., et al. 2011, *ApJS*, **192**, 5
- Annibali, F., Bressan, A., Rampazzo, R., Zeilinger, W. W., & Danese, L. 2007, *A&A*, **463**, 455
- Arnold, J. A., Romanowsky, A. J., Brodie, J. P., et al. 2014, *ApJ*, **791**, 80
- Asplund, M., Grevesse, N., Sauval, A. J., & Scott, P. 2009, *ARA&A*, **47**, 481
- Baes, M., Sil'chenko, O. K., Moiseev, A. V., & Manakova, E. A. 2007, *A&A*, **467**, 991
- Barro, G., Faber, S. M., Pérez-González, P. G., et al. 2013, *ApJ*, **765**, 104
- Beers, T. C., Flynn, K., & Gebhardt, K. 1990, *AJ*, **100**, 32
- Bender, R., Burstein, D., & Faber, S. M. 1993, *ApJ*, **411**, 153
- Bender, R., Kormendy, J., Cornell, M. E., & Fisher, D. B. 2014, *ApJ*, submitted (arXiv:1411.2598)
- Bernardi, M., Hyde, J. B., Sheth, R. K., Miller, C. J., & Nichol, R. C. 2007, *AJ*, **133**, 1741
- Bernardi, M., Nichol, R. C., Sheth, R. K., Miller, C. J., & Brinkmann, J. 2006, *AJ*, **131**, 1288
- Blanc, G. A., Heiderman, A., Gebhardt, K., Evans, N. J., II, & Adams, J. 2009, *ApJ*, **704**, 842
- Blanc, G. A., Weinzirl, T., Song, M., et al. 2013, *AJ*, **145**, 138
- Brough, S., Proctor, R., Forbes, D. A., et al. 2007, *MNRAS*, **378**, 1507
- Bundy, K., Bershady, M. A., Law, D. R., et al. 2015, *ApJ*, **798**, 7
- Burstein, D. 1985, *PASP*, **97**, 89
- Caon, N., Capaccioli, M., & D'Onofrio, M. 1993, *MNRAS*, **265**, 1013
- Cappellari, M., & Emsellem, E. 2004, *PASP*, **116**, 138
- Cappellari, M., Bacon, R., Bureau, M., et al. 2006, *MNRAS*, **366**, 1126
- Cappellari, M., McDermid, R. M., Alatalo, K., et al. 2012, *Nature*, **484**, 485
- Carollo, C. M., & Danziger, I. J. 1994, *MNRAS*, **270**, 743
- Carollo, C. M., Danziger, I. J., & Buson, L. 1993, *MNRAS*, **265**, 553
- Cenarro, A. J., Sánchez-Blázquez, P., Cardiel, N., & Gorgas, J. 2004, *ApJL*, **614**, L101
- Choi, J., Conroy, C., Moustakas, J., et al. 2014, *ApJ*, **792**, 95
- Clemens, M. S., Bressan, A., Nikolic, B., & Rampazzo, R. 2009, *MNRAS*, **392**, L35
- Coccatto, L., Gerhard, O., & Arnaboldi, M. 2010, *MNRAS*, **407**, L26
- Coccatto, L., Gerhard, O., Arnaboldi, M., & Ventimiglia, G. 2011, *A&A*, **533**, A138
- Cohen, J. G. 1979, *ApJ*, **228**, 405
- Cohen, J. G., Briley, M. M., & Stetson, P. B. 2005, *AJ*, **130**, 1177
- Conroy, C., Graves, G. J., & van Dokkum, P. G. 2014, *ApJ*, **780**, 33
- Conroy, C., & van Dokkum, P. 2012, *ApJ*, **747**, 69
- Cooper, M. C., Coil, A. L., Gerke, B. F., et al. 2010, *MNRAS*, **409**, 337
- Crojević, D., Ferguson, A. M. N., Irwin, M. J., et al. 2013, *MNRAS*, **432**, 832
- Crook, A. C., Huchra, J. P., Martimbeau, N., et al. 2007, *ApJ*, **655**, 790
- Croom, S. M., Lawrence, J. S., Bland-Hawthorn, J., et al. 2012, *MNRAS*, **421**, 872
- Dressler, A. 1980, *ApJS*, **42**, 565
- Dunkley, J., Spergel, D. N., Komatsu, E., et al. 2009, *ApJ*, **701**, 1804
- Emsellem, E., Cappellari, M., Peletier, R. F., et al. 2004, *MNRAS*, **352**, 721
- Faber, S. M., Burstein, D., & Dressler, A. 1977, *AJ*, **82**, 941
- Faber, S. M., Friel, E. D., Burstein, D., & Gaskell, C. M. 1985, *ApJS*, **57**, 711
- Ferrarese, L., Côté, P., Jordán, A., et al. 2006, *ApJS*, **164**, 334
- Fisher, D., Franx, M., & Illingworth, G. 1995, *ApJ*, **448**, 119
- Gallazzi, A., Charlot, S., Brinchmann, J., White, S. D. M., & Tremonti, C. A. 2005, *MNRAS*, **362**, 41
- Gorgas, J., Efstathiou, G., & Aragon Salamanca, A. 1990, *MNRAS*, **245**, 217
- Graves, G. J., Faber, S. M., & Schiavon, R. P. 2009, *ApJ*, **693**, 486
- Graves, G. J., Faber, S. M., & Schiavon, R. P. 2010, *ApJ*, **721**, 278
- Graves, G. J., Faber, S. M., Schiavon, R. P., & Yan, R. 2007, *ApJ*, **671**, 243
- Graves, G. J., & Schiavon, R. P. 2008, *ApJS*, **177**, 446
- Greene, J. E., Murphy, J. D., Comerford, J. M., Gebhardt, K., & Adams, J. J. 2012, *ApJ*, **750**, 32
- Greene, J. E., Murphy, J. D., Graves, G. J., et al. 2013, *ApJ*, **776**, 64
- Harris, G. L. H., Harris, W. E., & Poole, G. B. 1999, *AJ*, **117**, 855
- Harris, W. E., Harris, G. L. H., Layden, A. C., & Wehner, E. M. H. 2007, *ApJ*, **666**, 903
- Henry, R. B. C., Edmunds, M. G., & Köppen, J. 2000, *ApJ*, **541**, 660
- Hill, G. J., MacQueen, P. J., Smith, M. P., et al. 2008, *Proc. SPIE*, **7014**, 701470
- Hirschmann, M., Naab, T., Ostriker, J. P., et al. 2015, *MNRAS*, **449**, 528
- Huchra, J. P., Macri, L. M., Masters, K. L., et al. 2012, *ApJS*, **199**, 26
- Jarrett, T. H., Chester, T., Cutri, R., Schneider, S. E., & Huchra, J. P. 2003, *AJ*, **125**, 525
- Jimmy, Tran, K.-V., Brough, S., et al. 2013, *ApJ*, **778**, 171
- Johansson, J., Thomas, D., & Maraston, C. 2012, *MNRAS*, **421**, 1908
- Kalirai, J. S., Gilbert, K. M., Guhathakurta, P., et al. 2006, *ApJ*, **648**, 389
- Kelson, D. D. 2003, *PASP*, **115**, 688
- Kelson, D. D., Illingworth, G. D., Franx, M., & van Dokkum, P. G. 2006, *ApJ*, **653**, 159
- Kirby, E. N., Guo, M., Zhang, A. J., et al. 2015, *ApJ*, **801**, 125
- Ko, J., & Im, M. 2005, *JKAS*, **38**, 149
- Kobayashi, C. 2004, *MNRAS*, **347**, 740
- Kobayashi, C., & Arimoto, N. 1999, *ApJ*, **527**, 573
- Kormendy, J., Fisher, D. B., Cornell, M. E., & Bender, R. 2009, *ApJS*, **182**, 216
- Korn, A. J., Maraston, C., & Thomas, D. 2005, *A&A*, **438**, 685
- Kuntschner, H., Smith, R. J., Colless, M., et al. 2002, *MNRAS*, **337**, 172
- Kuntschner, H., Emsellem, E., Bacon, R., et al. 2010, *MNRAS*, **408**, 97
- La Barbera, F., de Carvalho, R. R., Gal, R. R., et al. 2005, *ApJL*, **626**, L19
- La Barbera, F., Ferreras, I., de Carvalho, R. R., et al. 2012, *MNRAS*, **426**, 2300
- La Barbera, F., Pasquali, A., Ferreras, I., et al. 2014, *MNRAS*, **445**, 1977
- Lackner, C. N., & Gunn, J. E. 2012, *MNRAS*, **421**, 2277
- Lackner, C. N., & Gunn, J. E. 2013, *MNRAS*, **428**, 2141
- Lauer, T. R., Faber, S. M., Richstone, D., et al. 2007, *ApJ*, **662**, 808
- Ma, C.-P., Greene, J. E., McConnell, N., et al. 2014, *ApJ*, **795**, 158
- Maeder, A. 1992, *A&A*, **264**, 105
- Magnier, E. A., Schlafly, E., Finkbeiner, D., et al. 2013, *ApJS*, **205**, 20
- Mandelbaum, R., Hirata, C. M., Seljak, U., et al. 2005, *MNRAS*, **361**, 1287
- McConnell, N. J., Ma, C.-P., Murphy, J. D., et al. 2012, *ApJ*, **756**, 179
- McDermid, R. M., Alatalo, K., Blitz, L., et al. 2015, *MNRAS*, **448**, 3484
- Mehlert, D., Thomas, D., Saglia, R. P., Bender, R., & Wegner, G. 2003, *A&A*, **407**, 423
- Murphy, J. D., Gebhardt, K., & Adams, J. J. 2011, *ApJ*, **729**, 129
- Naab, T., Johansson, P. H., & Ostriker, J. P. 2009, *ApJL*, **699**, L178
- Naab, T., Oser, L., Emsellem, E., et al. 2014, *MNRAS*, **444**, 3357
- Newman, A. B., Ellis, R. S., Bundy, K., & Treu, T. 2012, *ApJ*, **746**, 162
- Ogando, R. L. C., Maia, M. A. G., Chiappini, C., et al. 2005, *ApJL*, **632**, L61
- Oliveira-Altamirano, P., Brough, S., Jimmy, et al. 2015, *MNRAS*, **449**, 3347
- Oser, L., Naab, T., Ostriker, J. P., & Johansson, P. H. 2012, *ApJ*, **744**, 63
- Oser, L., Ostriker, J. P., Naab, T., Johansson, P. H., & Burkert, A. 2010, *ApJ*, **725**, 2312
- Pasquali, A., Gallazzi, A., Fontanot, F., et al. 2010, *MNRAS*, **407**, 937
- Pastorello, N., Forbes, D. A., Foster, C., et al. 2014, *MNRAS*, **442**, 1003
- Patel, S. G., van Dokkum, P. G., Franx, M., et al. 2013, *ApJ*, **766**, 15
- Patuel, G., Petit, C., Prugniel, P., et al. 2003, *A&A*, **412**, 45
- Peacock, M. B., Strader, J., Romanowsky, A. J., & Brodie, J. P. 2015, *ApJ*, **800**, 13
- Peletier, R. F., Vazdekis, A., Arribas, S., et al. 1999, *MNRAS*, **310**, 863
- Price, J., Philipps, S., Huxor, A., Smith, R. J., & Lucey, J. R. 2011, *MNRAS*, **411**, 2558
- Proctor, R. N., & Sansom, A. E. 2002, *MNRAS*, **333**, 517
- Pu, S.-B., & Han, Z.-W. 2011, *RAA*, **11**, 909

- Pu, S. B., Saglia, R. P., Fabricius, M. H., et al. 2010, *A&A*, **516**, A4
- Raskutti, S., Greene, J. E., & Murphy, J. D. 2014, *ApJ*, **786**, 23
- Rawle, T. D., Smith, R. J., Lucey, J. R., & Swinbank, A. M. 2008, *MNRAS*, **389**, 1891
- Rejkuba, M., Greggio, L., Harris, W. E., Harris, G. L. H., & Peng, E. W. 2005, *ApJ*, **631**, 262
- Röttgers, B., Naab, T., & Oser, L. 2014, *MNRAS*, **445**, 1065
- Saglia, R. P., Maraston, C., Thomas, D., Bender, R., & Colless, M. 2002, *ApJL*, **579**, L13
- Salasnich, B., Girardi, L., Weiss, A., & Chiosi, C. 2000, *A&A*, **361**, 1023
- Sánchez, S. F., Kennicutt, R. C., Gil de Paz, A., et al. 2012, *A&A*, **538**, A8
- Sánchez-Blázquez, P., Forbes, D. A., Strader, J., Brodie, J., & Proctor, R. 2007, *MNRAS*, **377**, 759
- Sánchez-Blázquez, P., Gorgas, J., Cardiel, N., & González, J. J. 2006, *A&A*, **457**, 787
- Sarzi, M., Falcón-Barroso, J., Davies, R. L., et al. 2006, *MNRAS*, **366**, 1151
- Sarzi, M., Shields, J. C., Schawinski, K., et al. 2010, *MNRAS*, **402**, 2187
- Schiavon, R. P. 2007, *ApJS*, **171**, 146
- Schlafly, E. F., Finkbeiner, D. P., Jurić, M., et al. 2012, *ApJ*, **756**, 158
- Serven, J., Worthey, G., & Briley, M. M. 2005, *ApJ*, **627**, 754
- Skrutskie, M. F., Cutri, R. M., Stiening, R., et al. 2006, *AJ*, **131**, 1163
- Smith, R. J., Lucey, J. R., Hudson, M. J., & Bridges, T. J. 2009, *MNRAS*, **398**, 119
- Spinrad, H., & Taylor, B. J. 1971, *ApJS*, **22**, 445
- Spolaor, M., Kobayashi, C., Forbes, D. A., Couch, W. J., & Hau, G. K. T. 2010, *MNRAS*, **408**, 272
- Strateva, I., Ivezić, Ž., Knapp, G. R., et al. 2001, *AJ*, **122**, 1861
- Tang, B., Worthey, G., & Davis, A. B. 2014, *MNRAS*, **445**, 1538
- Terlevich, A. I., & Forbes, D. A. 2002, *MNRAS*, **330**, 547
- Terlevich, E., Diaz, A. I., & Terlevich, R. 1990, *MNRAS*, **242**, 271
- Thomas, D., Maraston, C., & Bender, R. 2003, *MNRAS*, **339**, 897
- Thomas, D., Maraston, C., Bender, R., & Mendes de Oliveira, C. 2005, *ApJ*, **621**, 673
- Thomas, D., Maraston, C., Schawinski, K., Sarzi, M., & Silk, J. 2010, *MNRAS*, **404**, 1775
- Thomas, J., Saglia, R. P., Bender, R., et al. 2011, *MNRAS*, **415**, 545
- Tonry, J. L., Stubbs, C. W., Lykke, K. R., et al. 2012, *ApJ*, **750**, 99
- Trager, S. C., Faber, S. M., Worthey, G., & González, J. J. 2000a, *AJ*, **120**, 165
- Trager, S. C., Faber, S. M., Worthey, G., & González, J. J. 2000b, *AJ*, **119**, 1645
- Trager, S. C., Worthey, G., Faber, S. M., Burstein, D., & González, J. J. 1998, *ApJS*, **116**, 1
- Tripicco, M. J., & Bell, R. A. 1995, *AJ*, **110**, 3035
- Valentinuzzi, T., Fritz, J., Poggianti, B. M., et al. 2010, *ApJ*, **712**, 226
- van den Bosch, R. C. E., Gebhardt, K., Gültekin, K., Yıldırım, A., & Walsh, J. L. 2015, *ApJS*, **218**, 10
- van der Wel, A., Franx, M., van Dokkum, P. G., et al. 2014, *ApJ*, **788**, 28
- van der Wel, A., Holden, B. P., Zirm, A. W., et al. 2008, *ApJ*, **688**, 48
- van Dokkum, P. G., Franx, M., Kriek, M., et al. 2008, *ApJ*, **677**, L5
- Vazdekis, A., Peletier, R. F., Beckman, J. E., & Casuso, E. 1997, *ApJS*, **111**, 203
- Vazdekis, A., Sánchez-Blázquez, P., Falcón-Barroso, J., et al. 2010, *MNRAS*, **404**, 1639
- Wake, D. A., van Dokkum, P. G., & Franx, M. 2012, *ApJL*, **751**, L44
- Weijmans, A.-M., Cappellari, M., Bacon, R., et al. 2009, *MNRAS*, **398**, 561
- White, S. D. M. 1980, *MNRAS*, **191**, 1P
- Williams, B. F., Dalcanton, J. J., Bell, E. F., et al. 2015, *ApJ*, **802**, 49
- Worthey, G. 1998, *PASP*, **110**, 888
- Worthey, G. 2004, *AJ*, **128**, 2826
- Worthey, G., Faber, S. M., & Gonzalez, J. J. 1992, *ApJ*, **398**, 69
- Worthey, G., Faber, S. M., Gonzalez, J. J., & Burstein, D. 1994, *ApJS*, **94**, 687
- Worthey, G., Ingermann, B. A., & Serven, J. 2011, *ApJ*, **729**, 148
- Worthey, G., Tang, B., & Serven, J. 2014, *ApJ*, **783**, 20
- Wu, X., Gerhard, O., Naab, T., et al. 2014, *MNRAS*, **438**, 2701
- Yan, R. 2011, *AJ*, **142**, 153
- Yan, R., & Blanton, M. R. 2012, *ApJ*, **747**, 61
- Yoachim, P., Roškar, R., & Debattista, V. P. 2010, *ApJL*, **716**, L4
- York, D. G., Adelman, J., Anderson, J. E., Jr., et al. 2000, *AJ*, **120**, 1579
- Zhu, G., Blanton, M. R., & Moustakas, J. 2010, *ApJ*, **722**, 491